Chemical Engineering Science 327 (2026) 123647

Contents lists available at ScienceDirect

Chemical Engineering Science

journal homepage: www.elsevier.com/locate/ces

A physics-based electrothermal fluidized bed reactor model applied to COS decomposition

Klaus Jacobs [a], Soroush Zareghorbaei [a], Jeroen Lauwaert [b], Joris W. Thybaut [a,*]

[a] Laboratory for Chemical Technology (LCT), Ghent University, Technologiepark 125, 9052 Ghent, Belgium
[b] Industrial Catalysis and Adsorption Technology (INCAT), Ghent University, Valentin Vaerwyckweg 1, 9000 Ghent, Belgium

ARTICLE INFO

Keywords:
Fluidized Bed Reactor
Direct Joule Heating
High temperature Reactor Electrification
Electric Current Partition Model
Laplacian Electric Field Model
COS decomposition

ABSTRACT

The electrification of high-temperature reactors is a promising strategy for reducing CO_2 emissions in energy-intensive industries. ElectroThermal Fluidized Bed (ETFB) reactors are particularly attractive due to their ability to supply distributed heat directly through Joule heating. However, reactor-scale models that consistently link electrical design variables to temperature and conversion profiles remain limited. In this work, a coupled electrical–thermal modelling framework for ETFB reactors is developed to address this need. A field-resolved Laplacian Field Model (LFM) is formulated to compute electric potential, current paths, and spatially distributed Joule heating under prescribed electrical properties, enabling detailed analysis of geometry-dependent heating patterns. To support rapid parametric exploration, a simplified Current Partition Model (CPM) based on resistor analogies is also introduced, capturing dominant trends in power distribution, temperature, and conversion at substantially reduced computational cost, while exhibiting systematic deviations under certain geometric conditions. The framework is applied to the highly endothermic thermal decomposition of carbonyl sulfide (COS), illustrating how electrode configuration governs Joule heating distribution and indirectly influences thermal and reactive behaviour. In addition, the thermal formulation is assessed using available steady-state ETFB operating data from the literature. From the reported power and temperature data, the bed resistivity and effective heat-loss parameters are estimated. With these values, the model reproduces the experimental electrode-tip temperatures within good accuracy across the range of immersion depths. Overall, the proposed methodology offers a structured reactor-scale approach to guide ETFB design and sizing, linking electrical configuration, heat demand, and conversion targets, while remaining compatible with future extensions.

1. Introduction

Electrification of energy-intensive processes and, more particularly of high-temperature reactors (>400 °C), is a key strategy for reducing CO_2 emissions in the chemical industry. The operation of such reactors is estimated to contribute to approximately 6% of the global CO_2 emissions (Saygin and Gielen, 2021) and 30% of emissions from the chemical industry (Energy Information Administration, 2024). Moreover, fuel consumption in these processes accounts for approximately 45% of the total energy demand. It is estimated that up to half of the fuel consumption in industrial processes operating at temperatures as high as 1000 °C, such as steam reforming and cracking in the oil industry, can be replaced by electricity using currently available technologies. However, at present, the electrification of higher-temperature processes remains at the research or pilot stage (McKinsey, 2025). Despite these hurdles, ongoing advancements in high-temperature electrification technologies, coupled with increasing availability of carbon–neutral electricity, could enable a transition to electrically powered reactors. If successfully scaled, this transition has the potential to substantially reduce greenhouse gas emissions in the chemical industry.

High-temperature waste-gas treatment provides a representative example of these challenges. Conventional acid gas treatment units, such as Claus reactors, operate at elevated temperatures where sulfur-containing gases undergo thermal and catalytic conversion. These processes rely almost exclusively on fossil-fired heating and suffer from low thermal efficiency due to radiative and convective losses inherent to externally heated reactors. As a result, they contribute notably to industrial CO_2 emissions while offering limited flexibility for integration with renewable electricity.

The EU-funded e-CODUCT project addresses this challenge by proposing an electrified alternative to conventional acid gas treatment. The

* Corresponding author.
E-mail address: Joris.Thybaut@UGent.be (J.W. Thybaut).

https://doi.org/10.1016/j.ces.2026.123647
Received 27 October 2025; Received in revised form 10 February 2026; Accepted 17 February 2026
Available online 18 February 2026

Nomenclature

Symbols

Symbol	Definition. Units
A_I	Cross-sectional area to the flow of electric current. m^2
Acr	Cross-sectional area of the reactor. m^2
a_I	Interfacial area per unit gas volume in the low-density phase. m^{-1}
As	Heat transfer surface area per reactor volume. m^{-1}
Cp_g	Gas heat capacity. kJ kg^{-1} K^{-1}
Cp_p	Particle heat capacity. kJ kg^{-1} K^{-1}
$C_{i,j}$	Concentration of species i in phase j. mol m^{-3}
d_b	Bubble diameter. m
d_p	Particle diameter. m
D_j	Axial dispersion coefficient in phase j. m^2 s^{-1}
dQ_{JH} dz^{-1}	Joule heating per unit height. kW m^{-1}
E_r	Radial component of the electric field. V m^{-1}
E_z	Axial component of the electric field. V m^{-1}
F_i	Molar flow of species i. mol s^{-1}
F_{i_j}	Molar flow of species i in phase j. mol s^{-1}
f_p	Fraction of particles that are lost due to entrainment. –
H_{exp}	Expanded bed height. m
h_{tot}	Total heat transfer coefficient. W m^{-2} K^{-1}
h_{top}	Top convective heat transfer coefficient. W m^{-2} K^{-1}
ΔH_{rxn}	Reaction enthalpy. kJ mol^{-1}
I	Electric current. A
I_{CAR}	Electric current through CAR. A
I_{TCR}	Electric current through TCR. A
J_J	Axial molar diffusive flux in phase j. mol m^{-2} s^{-1}
J	Current density. A m^{-2}
$\nabla \cdot J$	Divergence of electrical current density. A m^{-3}
J_r	Radial component of the current density. A m^{-2}
J_z	Axial component of the current density. A m^{-2}
$\overline{\overline{J_r}}$	Radial current density contribution to the magnitude of the current density. –
k_e	Effective thermal conductivity of the bed. kW m^{-1} K^{-1}
k_{LH}	Interphase mass transfer rate constant. m s^{-1}
mH	Enthalpy flow of gas. kW
m_{p0}	Initial mass of particles. kg
q	Axial heat conduction. W m^{-2}
q_L	Fraction of total gas flow passing through low-density phase. —
Q_{JH}	Heat generated due to Joule heating. kW
Q_{rxn}	Reaction enthalpy term. kW
r	Radial coordinate. m
r_1	Radius of the central electrode. m
r_2	Reactor radius. m
R	Electrical resistance. Ω
R_{bed}	Electrical resistance through the bed/Interelectrode resistance. Ω
R_{CAR}	Electrical resistance through CAR. Ω
R_{TCR}	Electrical resistance through TCR. Ω
$R_{i,k}$	volumetric reaction rate of reaction k. mol m^{-3} s^{-1}
R_{i,j,V_j}	Production/Consumption rate of species i in phase j. mol m^{-3} s^{-1}
s_{bed}	Bed resistivity. Ω-cm
T	Temperature. K / °C
T_{avg}	Average bed temperature. K / °C
T_w	Wall temperature. K / °C
t_r	Gas residence time. s
u	Gas superficial velocity. m s^{-1}
u_j	Superficial velocity in phase j. m s^{-1}
u_{cr}	Critical transition velocity from bubbling to turbulent regime. m s^{-1}
u_{mf}	Minimum fluidization velocity. m s^{-1}
ΔV	Electric potential. V
∇V	Electric potential gradient. V m^{-1}
V_{app}	Applied electric potential. V
X_{avg}	Average conversion. —
z	Axial coordinate. m
Δz	Axial height element. m
Z_1	Height between the distributor to the tip of the central electrode. m
Z_2	Height between the tip of the central electrode and the top of the bed. m

Greek Symbols

Symbol	Definition. Units
ε	Bed porosity. —
ε_j	Porosity of phase j. —
ε_{mf}	Porosity at minimum fluidization. —
μ_g	Gas viscosity. Pa s
ρ_g	Gas density. kg m^{-3}
ρ_p	Particle density. kg m^{-3}
Ψ_H	Volume fraction of high-density phase. —
Ψ_L	Volume fraction of low-density phase. —

Acronyms

Symbol	Definition. Units
CAR	Coaxial resistor.
CPM	Current Partition Model. —
LFM	Laplacian Field Model. —
ETFB	ElectroThermal Fluidized Bed. —
ESD	Electrode submersion depth. —
FBR	Fluidized Bed Reactor. —
PRWS	Peng–Robinson Wong–Sandler. —
CFD	Computational Fluid Dynamics. —
COS	Carbonyl sulfide. —
BVP	Boundary Value Problem. —
TEA	Techno economic analysis. —
TCR	Truncated cone resistor. —
LCA	Life cycle analysis. —
ICE	Immersion dept of Central Electrode. —

process converts CO_2 and H_2S into valuable products through a two-step pathway (e-CODUCT, 2025): CO_2 and H_2S are first converted to COS over a Na^+-zeolite catalyst (Fabbiani et al., 2024). The resulting COS then undergoes thermal decomposition to CO and elemental sulphur (Clark et al., 2001), a strongly endothermic step operating at approximately 800–1200 °C (Hay and Belford, 1967; Karan et al., 2005; Karan et al., 1998). These characteristics make COS decomposition a promising candidate for electrified operation and motivate the development of reactor configurations capable of delivering thermal energy by conversion of electricity into heat rather than relying on fossil based external heating.

Among the available electrification strategies, Joule (resistive) heating stands out due to its simplicity, high electrical-to-thermal efficiency, and ability to deliver heat directly within electrically conductive media (Siesing et al., 2018; Gupta and Sathiyamoorthy, 1999; Ahmed et al., 2024). This principle serves as a foundation to the operation of Electrothermal Fluidized Bed (ETFB) reactors, in which conductive particles act as the resistive medium that converts electrical power into heat within the bed. In contrast, several indirect electrification methods, such as electromagnetic induction and microwave heating, rely on

externally applied fields to generate heat within the reactor (Stankiewicz and Nigar, 2020). While these approaches offer attractive possibilities, microwave heating in particular suffers from shallow penetration depth and non-uniform energy distribution (Song et al., 2022; Atuonwu and Tassou, 2018), and plasma-based technologies present challenges related to durability, energy efficiency, and reactor-scale implementation (Seo et al., 2010; Gao et al., 2014; Idakiev et al., 2018). In contrast, Joule-heated electrothermal fluidized beds offer a robust and scalable route to deliver heat directly within the reacting medium, making them particularly attractive for high-temperature processes.

Compared to conventionally heated fluidized beds, such as those relying on external heating (fired furnaces) or internal heating elements (tube bundles), ETFB reactors offer several advantages. Notably, they exhibit very high energy efficiencies, ranging from 97% to 100%, characteristic of Joule-heated systems (Sakr and Liu, 2014). In contrast, fire-heated steam biomass gasification fluidized bed reactors achieve energy efficiencies of only 45% to 65% at temperatures between 650 °C and 950 °C (Feng et al., 2016). Additionally, ETFB reactors enable rapid heating rates of up to 1000 °C h^{-1} (Gao et al., 2014), allowing for precise temperature control. Furthermore, such reactors do not require internal heating elements, which could disrupt gas–solid interactions, or external heating elements, resulting in additional heat transfer resistances between the heating elements and the reactor content to be heated. Because of these advantages, electrothermal fluidization has been selected as the central technological pillar of the e-CODUCT project. A pilot-scale ETFB reactor is currently under construction to enable electrically powered COS decomposition under industrially relevant conditions.

Understanding the operating principles of an ETFB reactor is essential for explaining the origin of its advantages. An ETFB reactor integrates two well-established technologies: fluidization and Joule heating. It operates by applying a voltage difference (ΔV) across two electrodes, with a bed of electrically conductive particles serving as the medium through which the electric current flows. The conductive particles introduce electrical resistance to the current (I), generating heat via the Joule effect (Q_{JH}). When gas is introduced into the bed under conditions exceeding the minimum fluidization velocity, the solid particles transition from a packed state to a fluidized state, modifying the electric resistance (R) between the electrodes and enhancing both heat and mass transfer between the phases of the fluidized bed (Johnson, 1961). The effect of resistance changes with the power depends on how the power supply is regulated. Under constant-voltage operation, an increase in R leads to a decrease in I, and because $Q_{JH} = \Delta V^2 R^{-1}$, the power decreases. Under constant-current operation, an increase in R requires an increase in ΔV, and since $Q_{JH} = I^2 R$, the power increases.

ETFB reactors also present certain challenges. Fluidization increases the overall bed resistance compared to stagnant beds. This influences the reactor geometry and power supply requirements, meaning that even with particles of high intrinsic conductivity, achieving the desired heating power requires careful integration of reactor design and equipment selection for the intended application. Furthermore, the operating principle necessitates that both the electrodes and, in some cases, the reactor walls be electrically conductive, thereby restricting the choice of construction materials. Moreover, because heating occurs via direct resistive heating of the fluidized particles, temperature distribution may be non-uniform, leading to potential localized overheating or underheating of individual particles (Ahmed et al., 2024).

Different electrode configurations have been reported in the literature (Fig. 1) (Gupta and Sathiyamoorthy, 1999), including coaxial (Fig. 1A), parallel-plate (Fig. 1B), multi-electrode geometries (Fig. 1C) and end-to-end (Fig. 1D). These configurations influence current distribution, characteristic resistances, and resulting heating patterns within the bed. Coaxial designs typically exhibit low resistances (0.5–2 Ω), permitting low-voltage/high-current operation, whereas end-to-end systems operate at higher resistances (50–300 Ω), requiring high-voltage supplies but reducing current densities and electrode wear (Kavlick et al., 1971).

Despite their growing relevance for electrified reactor technologies, the mechanisms governing electrical conduction in fluidized beds remain only partially understood. Pioneering work by Goldschmidt and LeGoff (Goldschmidt and Le Goff, 1963) identified continuous particle–particle contact chains as the dominant conduction mechanism, with diffusion type charge transfer and particle arcing only playing secondary roles. Subsequent studies by Graham and Harvey (Graham and Harvey, 1965), Knowlton (Knowlton, 1971), and more recently by Fedorov et al. (Fedorov et al., 2016) indicated that micro-arcing may occur when contact chains break, although its quantitative contribution to overall conductivity remains uncertain. In parallel, efforts to characterize bed resistivity (s_{bed}) have produced empirical and semi-empirical correlations that relate resistivity to particle size, bed geometry, porosity, angle of repose, and hydrodynamic conditions (Pulsifer and Wheelock, 1978; Jones and Wheelock, 1970). Additional correlations for bed resistance under minimum-fluidization and bubbling conditions have been proposed (Goldschmidt and Le Goff, 1963; Gubinskyi et al., 2017), while more sophisticated models incorporating contact mechanics have been developed (Fedorov et al., 2016; Malinovskii et al., 2012), though they require parameters that are difficult to

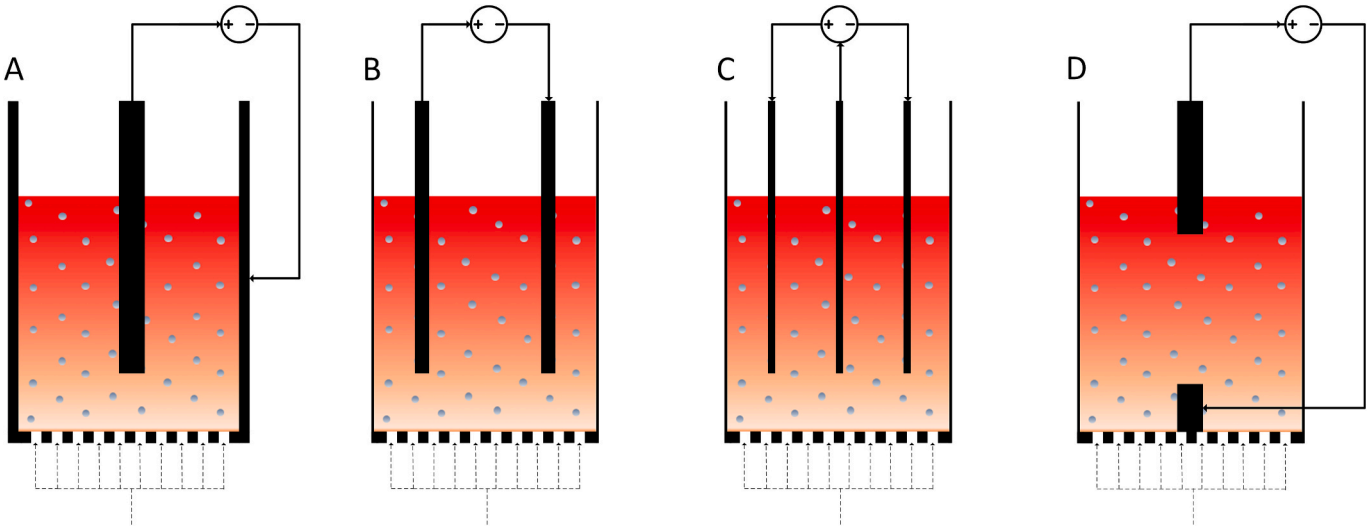

Fig. 1. Different electrode configurations in an ETFB: A – Coaxial electrode; B – Parallel plates; C – Multiple electrode; D – End-to-End.

estimate such as the contact pressure between two colliding particles, the estimated resilience of granular structure, contact area between particles and particle–particle contact footprint. As a result, accurate prediction of bed resistivity generally remains system-specific and often requires experimental calibration.

Research incorporating thermal effects is even more limited. Fedorov et al. (Fedorov et al., 2016) and Simeiko (Simeiko, 2018) presented general heat-balance formulations without spatial resolution, while Gubynski et al. (Gubynskyi et al., 2013) later introduced a one-dimensional radial model for coaxial ETFBs that accounts for resistive heating through an effective thermal conductivity term. However, axial temperature variations were not resolved, restricting its applicability to geometries where heat transfer occurs predominantly in the radial direction. Taken together, these studies provide valuable insight into electrical behavior within ETFBs but stop short of delivering a reactor-scale modelling framework capable of coupling electrical potential fields, Joule heat generation, hydrodynamics, and reactive gas–solid transport.

A critical gap therefore exists: no reactor-scale model for ETFBs is available in the literature. Existing publications address either isolated electrical properties or simplified heat balances, but none provides the governing equations, closure relations, or modelling strategy needed to simulate reactive, electrically heated fluidized beds. In contrast to fixed-bed or conventionally heated fluidized beds, where well-established non-isothermal reactor models serve as a foundation, ETFBs lack any comparable starting point. It is therefore necessary to develop a reactor-scale electrothermal model from first principles, integrating electrical, thermal, and hydrodynamic in a consistent mathematical framework.

Beyond filling a gap in the literature, establishing a reactor-scale heat balance that directly links electrical operating parameters, ΔV, I, and Q_{JH}, to the resulting temperature and conversion profiles is essential for both scientific and engineering purposes. Framed at the reactor scale, such a model enables physically interpretable analysis of electrothermal energy transfer in a fluidized bed and provides a qualitative design tool for assessing the influence of operating conditions, electrode configurations, and bed properties. This capability is crucial for formulating qualitative design guidelines and for the design, optimization, and scale-up of ETFB reactors, where spatially distributed heating, strong temperature sensitivities, and coupled electrical–thermal effects govern reactor performance.

Importantly, this work does not aim to develop or improve resistivity models for fluidized beds of conductive particles. Particle-level conduction physics, including collision pressures, surface contact mechanics, and micro-arcing, operate at scales far remote from the reactor level and cannot be reliably predicted without detailed experimental characterization or numerical estimation of parameters, neither of which is required for the reactor-scale framework developed here. The accuracy of reactor-scale predictions depends on the availability of such data, and continued research on electrical resistivity in fluidized beds remains essential.

To keep the scope aligned with the general objective of establishing a physically grounded reactor-scale formulation, s_{bed} and the expanded bed height (H_{exp}) should be treated as prescribed input quantities rather than variables to be solved. Predicting their spatial or temporal dependence would require incorporating particle-scale conduction physics, temperature and pressure dependent contact networks, or hydrodynamic expansion models, complexities that cannot be meaningfully accounted for without dedicated experiments and lie outside the purpose of the present work. By fixing these properties, the model isolates the essential electrothermal coupling at the reactor scale and provides a clear derivation of the governing equations. Importantly, the framework developed here is intentionally foundational: it establishes the core electrothermal and reactive transport structure from which more advanced ETFB models, including those with variable resistivity, dynamic bed expansion, or fully resolved multiphase hydrodynamics, can be systematically derived in future work.

Guided by these requirements, the objective of this work is to establish a reactor-scale electrothermal modelling framework that couples: (i) a physics-based electrical model describing electric-potential distribution and Joule heat generation, formulated either through a two-dimensional Laplacian Field Model (LFM) or a simplified Current Partition Model (CPM); (ii) two-phase (low- and high-density) mass balances for reactive flow; (iii) an idealized one-dimensional axial heat balance incorporating Joule heating and effective bed thermal conductivity, serving as a baseline from which practical ETFB models can be derived; and (iv) an initial validation of the thermal predictions against ETFB operating data retrieved from literature (Ahmed et al., 2025). This framework provides a methodological basis for qualitative design of ETFB reactors and for future experimental validation.

2. Development of the electrothermal fluidized bed reactor modeling framework

This section establishes the modelling framework used to describe the Electrothermal Fluidized Bed reactor at the reactor scale. It begins by defining the physical and simplifying assumptions on which the formulation is based (Section 2.1), after which the governing mass and heat balances are derived for the ETFB reactor (Sections 2.2 and 2.3). Finally, Section 2.4 integrates these relationships into the numerical solution strategy,

2.1. Modeling assumptions

The Electrothermal Fluidized Bed (ETFB) reactor model is formulated at the reactor scale and couples gas–solid hydrodynamics, axial heat transfer, and Joule heating. The modelling depth was chosen to resolve axial temperature and composition profiles, while avoiding the additional complexity associated with particle-scale electrical conduction models or full multiphase CFD. All constitutive equations and correlations used to evaluate hydrodynamic, transport, and thermophysical properties are provided in the Supplementary Information.

The reactor is assumed to operate under steady-state, isobaric, and adiabatic conditions. Gas–solid flow is represented using the two-phase bubbling model, comprising a high-density emulsion phase and a low-density bubble phase that is assumed essentially devoid of solids (ε_L = 97.5%). For clarity, the dense (high-density) phase represents the emulsion zone rich in solids, while the low-density phase corresponds to gas bubbles rising through the bed. Phase holdups and material balances are taken as constant along the reactor height. The dense phase is assumed to remain at minimum fluidization, providing a consistent hydrodynamic basis for correlations of porosity, minimum fluidization velocity, and interphase mass transfer. A fixed expanded bed height (H_{exp}) was used for all simulated cases; although real systems exhibit bed-height variation due to attrition, entrainment, or different gas velocities, fixing H_{exp} isolates the influence of electrical and thermal parameters in the present framework.

Radial gradients of species concentration and temperature are neglected (Yoshida and Kunii, 1968; Kunii et al., 2013), and departures from ideal plug flow are represented through axial dispersion in both phases. All thermophysical properties (gas density, viscosity, heat capacity, and thermal conductivity) and the superficial gas velocity were evaluated at an average bed temperature and composition. Introducing a spatially varying velocity field would require solving an additional momentum balance and embedding $u(z)$ within the convective transport terms, which lies beyond the reactor-scale scope of this work.

Gas and solids are assumed to be in local thermal equilibrium at the reactor scale, consistent with the high gas–solid heat-transfer coefficients characteristic of bubbling fluidized beds (Abba et al., 2003). A typical interphase heat transfer coefficient is in the order of $6\text{x}10^5$ W m^{-3} K^{-1} (Lungu et al., 2014), a simplified heat transfer analysis estimate shows that even under strongly endothermic conditions the resulting gas–solid temperature difference remains limited. For representative

reactor-scale gas-phase reaction rates (0.1-10mol m^{-3} s^{-1}) and a strongly endothermic heat of reaction of 300 kJ mol^{-1}, the implied interphase temperature difference remains in a 1–2 K range which is ≪1% of typical high temperature fluidized beds. Even for rates at an order of magnitude higher, the interphase temperature difference remains < 5% of the bed temperature. Accordingly, a single effective, cross-section-averaged temperature field is used to represent both phases, and no explicit interphase heat-transfer term is included. This one-dimensional formulation captures the dominant heat-transfer mechanisms relevant for reactor-scale assessment, while neglecting localized gas–solid thermal non-equilibrium effects.

COS decomposition is treated as a homogeneous, high-temperature gas-phase reaction. The reaction is considered to proceed thermally in both phases, and source terms are expressed per unit volume while catalytic effects are assumed to be negligible, as their role remain debated in the literature (Hay and Belford, 1967; Karan et al., 2005; Karan et al., 1998; Oya et al., 1994; Schecker and Wagner, 1969; Woiki and Roth, 1992; Partington and Neville, 1951; Haas and Khalafalla, 1973; Akimoto et al., 1986). The kinetic expressions, kinetic parameters, and standard reaction enthalpies employed in this work are compiled in the Supplementary Information.

Together, these assumptions were selected preserve the essential transport and reaction characteristics of the ETFB reactor while avoiding the complexity associated with solving a fully coupled multiphysics model.

2.2. ETFB reactor mass balances

The species balances in the ETFB reactor were formulated using the classical two-phase bubbling fluidized bed model, which distinguishes between a low-density bubble phase and a high-density emulsion phase (Abba et al., 2003). Each phase carries its own molar flow of species $Fi_{,L}$ and $F_{i,H}$ and is characterized by phase-specific superficial velocities (u_L, u_H), concentrations ($C_{i,L}$, $C_{i,H}$), axial flux (J_L, J_H), and volumetric homogeneous reaction rates (R_{i,L,V_L},R_{i,H,V_H}). Mass exchange between phases is represented by an interphase transfer term ($k_{LH}a_I$). A schematic illustrating the transport processes in both phases is shown in Fig. 2.

Because the emulsion is assumed to operate at minimum fluidization and the voidage of the bubble phase is specified (Section 2.1), the phase volume fractions (ψ_L, ψ_H) and gas holdups (ε_L, ε_H) were obtained directly from the overall material balance relationships of the two-phase model. Under these conditions, the Thompson et al. relationships (Thompson et al., 1999) reduce to explicit expressions for phase holdups and velocities, avoiding the need to solve a coupled nonlinear algebraic system together with the differential species balances. This greatly simplifies the reactor-scale formulation while remaining consistent with standard hydrodynamic correlations. The full derivation and explicit expressions are provided in the Supplementary Information.

The high and low density phase mass balances are given by Eqs. (1) and (2), respectively.

$$\frac{dF_{iH}}{dz} - \varepsilon_H R_{iH,V_H}\psi_H A_{cr} - \frac{D_H}{u_H}\frac{d^2F_{i,H}}{dz^2} + k_{LH}a_I\psi_L\left(\frac{F_{iH}}{\psi_H u_H} - \frac{F_{iL}}{\psi_L u_L}\right) = 0 \quad (1)$$

$$\frac{dF_{iL}}{dz} - \varepsilon_L R_{iL,V_L}\psi_L A_{cr} - \frac{D_L}{u_L}\frac{d^2F_{i,L}}{dz^2} + k_{LH}a_I\psi_L\left(\frac{F_{iL}}{\psi_L u_L} - \frac{F_{iH}}{\psi_H u_H}\right) = 0 \quad (2)$$

with the following boundary conditions for both phases where i represents the compound and j the phase.

$$\text{At } z = 0$$

$$\frac{F_{i,j} - F_{0i,j}}{\psi_j A_{cr}} = \frac{D_j}{\psi_j A_{cr} u_j}\frac{dF_{i,j}}{dz}$$

$$\text{At } z = H_{exp}$$

$$\frac{dF_{i,j}}{dz} = 0$$

Thermophysical properties required for evaluating transport and reaction terms were derived from Aspen Plus using the PRWS method for pure species (Wong and Sandler, 1992), and mixture properties were obtained with standard mixing rules from Reid et al. (Reid et al., 1987). The dense-phase dispersion coefficient D_H was estimated using the Bi and Grace correlation (Bi and Grace, 1997), consistent with the typical range of axial dispersion values reported for bubbling beds (10^{-3} to 10^{-1} m^2 s^{-1} (Zhang et al., 2009). Bubble-phase dispersion D_L was taken as the molecular diffusivity of the gas mixture (10^{-5} m^2 s^{-1}) (Thompson et al., 1999), although values up to 10^{-3} m^2 s^{-1} have been reported under vigorous bubbling (Breault, 2006). Bed porosity was obtained using the correlation of Clift and Grace (Clift and Grace, 1985), the minimum fluidization velocity from Abrahamsen and Geldart (Abrahamsen and Geldart, 1980) and bubble diameter from Agu et al. (Agu et al., 2018) necessaries for the estimation of volume and flow phase fractions. Interphase mass transfer coefficients were evaluated using the Sit and Grace expression (Sit and Grace, 1981).

Together, these balances determine the axial evolution of $F_{i,L}$ and $F_{i,H}$, whose sum provides the overall molar flow $F_i = F_{i,L} + F_{i,H}$ while the global species production/consumption rate follows $R_{i,v} = \psi_L R_{i,L,V_L} + \psi_H R_{i,H,V_H}$ required by the heat balance in Section 2.3.

2.3. ETFB reactor heat balance

The heat balance, illustrated in Fig. 3, accounts for volumetric Joule heating (dQ_{JH}), axial heat conduction (q), enthalpy transport by gas flow ($\dot{m}H$), and the reaction enthalpy term (Q_{rxn}). These terms form the basis

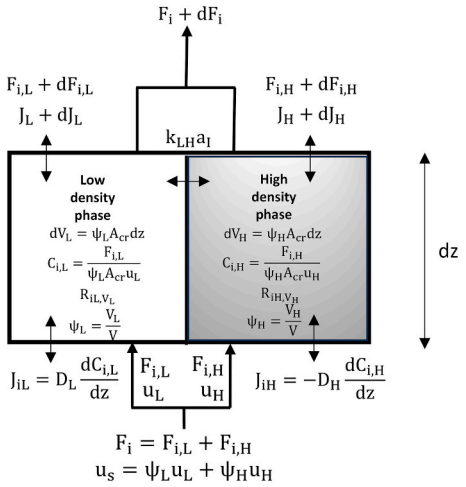

Fig. 2. 2-phase bubbling fluidized bed mass balance.

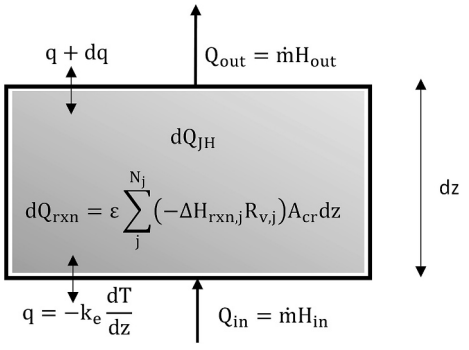

Fig. 3. Adiabatic ETFB reactor differential heat balance.

of the reactor's energy balance and are mapped directly in the schematic representation.

The heat balance equations for an infinitesimally small height element are presented in Eq. (3).

$$u\rho_g Cp_g \frac{dT}{dz} - k_e \frac{d^2T}{dz^2} - \varepsilon \sum_j^{N_j} \left(-\Delta H_{rxn} R_{v,k} \right) - \frac{\mathbf{dQ_{JH}}}{\mathbf{dzA_{cr}}} = 0 \quad (3)$$

The Joule heating term $dQ_{JH}\ dz^{-1}\ Acr^{-1}$ represents the volumetric distributed heat input obtained from the electrical model and depends on the electrode configuration.

In the case of a wall-heated fluidized bed, the last term in Eq. (3) representing Joule heating is replaced by a wall heat transfer term of the form $h_{tot}A_s(T_w - T)$.

With the following boundary conditions:

$$\text{At } z = 0$$

$$uA_{cr}Cp_g\rho_g(T_0 - T) = -k_e \frac{dT}{dz}$$

$$\text{At } z = H_{exp}$$

$$\frac{dT}{dz} = 0$$

The effective thermal conductivity of the fluidized bed (k_e) was determined based on an analogy between heat and mass transfer, as previously described by Abba (Abba, 2001). The effective thermal conductivity accounts for contributions from particle-to-particle conduction, gas-phase conduction, and convective effects arising from particle movement.

2.4. Numerical solution strategy and iterative coupling procedure

The coupled mass and heat balance equations constituted a BVP the solution of which required several quantities that are not known a priori. In particular, the average bed temperature T_{avg} and the average conversion X_{avg} had to be specified in order to evaluate mixture thermophysical properties, gas density, superficial velocity, and bed hydrodynamic parameters. Because these parameters depend on the solution itself, the model was solved through an outer iterative procedure that enforces consistency between the assumed and computed averages.

Once the fixed model inputs were defined, an initial estimate for T_{avg} was assumed, from which the thermophysical properties of the pure components and gas mixture (density, heat capacity, viscosity, thermal conductivity) were calculated using the correlations described in the Supplementary Information. At the same time, bed hydrodynamic quantities, including porosity, phase velocities, dispersion coefficients, and bubble characteristics, were evaluated based on this assumed average state.

To provide the boundary value problem solver with a physically meaningful initial guess, an isothermal two-phase mass balance that neglects axial dispersion was first solved using SciPy's solve_ivp routine. This preliminary calculation yielded approximate profiles for the molar flow rates $F_{i,H}(z)$ and $F_{i,L}(z)$. The initial temperature profile supplied to the BVP solver was taken as a uniform array equal to the assumed T_{avg}.

The complete set of governing equations, comprising the mass balances for both phases and the axial heat balance, was then solved simultaneously using SciPy's solve_bvp. The spatial Joule heating term $dQ_{JH}\ dz^{-1}$ was provided by the electrical model, and all transport and closure relations were evaluated using the expressions reported in the Supplementary Information.

Following each BVP solution, a new estimate of the average bed temperature was obtained from the predicted temperature profile, and the resulting outlet composition was used to update the average conversion. These updated values were compared against those assumed at the beginning of the iteration. If the difference exceeds the prescribed tolerance, thermophysical and hydrodynamic properties were recalculated using the updated averages, new initial guesses were generated, and the BVP is solved again. This outer loop continued until the assumed and computed values of T_{avg} converge.

When H_{exp} is not known in advance, it is updated after each iteration using: $H_{exp} = \frac{m_{p0}(1-f_p)}{\rho_p(1-\varepsilon)A_{cr}}$. Because this update is performed outside the BVP solution, no additional nonlinear algebraic constraints are introduced into the differential system.

This iterative numerical strategy ensured full internal consistency between the bed hydrodynamics, thermophysical properties, electrical heating profile, and the resulting axial temperature and conversion fields.

2.5. Development of Joule heating expression in an ETFB reactor model

Heat transfer in wall-heated fluidized bed reactors has been extensively investigated (Chen et al., 2005), leading to the development of several correlations for h_{tot} and a well-established understanding of its order of magnitude. To solve Eq. (3), one can estimate h_{tot} and T_w, enabling an engineering analysis of such reactors. However, this approach does not directly apply to the ETFB reactor heat balance model. In Eq. (3), no established formulation is available at present for the Joule heating term over an infinitesimal height element of the bed for a given input, such as voltage or current.

For the electrical model, s_{bed} is treated as a constant input parameter, fixed at 10 Ω·cm for all simulations. This value is representative of high-temperature graphite-based fluidized beds (Fedorov et al., 2016) and was adopted here to isolate the effects of reactor geometry and electrode configuration from uncertainties in particle-level conduction physics. Treating s_{bed} as fixed avoids introducing an additional modelling degree of freedom that cannot be reliably resolved without specific resistivity measurements. Contact resistances at the electrode–bed and bed–wall interfaces were neglected, and the potential contribution of (micro)-arcing was also ignored, an assumption consistent with earlier ETFB electrical studies (Goldschmidt and Le Goff, 1963; Knowlton, 1971; Fedorov et al., 2016) and justified by the reactor-scale focus of this work. The electrodes were assumed perfectly conducting, and the reactor wall was assigned its appropriate electrical boundary condition. Under these assumptions, the electric field was decoupled from bed hydrodynamics and enters the model solely through the distributed Joule heat generation term.

2.5.1. Laplacian field model

To derive an expression for the Joule heating term ($dQ_{JH}\ dz^{-1}$) in Eq. (3), a fundamental understanding of the electrical behavior within the fluidized bed is required. To the best of our knowledge, no detailed experimental or modeling studies have systematically addressed this specific topic. Nevertheless, it was crucial to obtain an objective representation of the bed's electrical behavior, while maintaining physical significance. To achieve this, a two-dimensional Laplacian field model (LFM) in cylindrical coordinates, as expressed in Eq. (4) and based on Knowlton's approach (Knowlton, 1971), was used to solve for the electric potential field while neglecting arcing in the bed and contact resistances. Eq. (4) was derived from the charge conservation principle ($\nabla \cdot J = 0$) and Ohm's law ($J = -s_{bed}^{-1} \nabla V$) under constant resistivity assumption and cylindrical coordinates.

$$\frac{d^2\Delta V}{dr^2} + \frac{1}{r}\frac{d\Delta V}{dr} + \frac{d^2\Delta V}{dz^2} = 0 \quad (4)$$

The following boundary conditions were applied to the geometry shown in Fig. 1A with conductive distributor.

$$\text{At } r = r_1 \text{ and } Z_1 \le z \le Z_2$$

$$\Delta V = \Delta V_{app}$$

$$\text{At } z = Z_1 \text{ and } 0 \le r \le r_1$$

$$\Delta V = \Delta V_{app}$$

$$\text{At } z = 0 \text{ and } 0 \le r \le r_2$$

$$\Delta V = 0$$

$$\text{At } r = r_1 \text{ and } 0 \le z \le Z_2$$

wall, respectively. Z_1 is the distance between the bottom to the tip of the electrode and Z_2 is the height between the electrode tip and the expended bed surface. The chosen coaxial ETFB reactor geometry with a conductive distributor was selected as a representative case that balances computational efficiency and physical relevance. Additionally, its relatively simple boundary conditions enable a more manageable mathematical formulation while still capturing the essential electrical phenomena governing charge transport and Joule heating in the system. While this work specifically applies the methodology to a coaxial ETFB reactor, the approach is generalizable and can be extended to other geometries with appropriate modifications to the boundary conditions and numerical discretization.

$$u\rho_g Cp_g \frac{dT}{dz} - k_e \frac{d^2T}{dz^2} - \varepsilon \sum_j^{N_j} \left(-\Delta H_{rxn} R_{v,j}\right) - \frac{\left(\int_0^{r_2}\int_0^{2\pi} -\frac{1}{s_{bed}}\left(\left(\frac{d\Delta V}{dr}\right)^2 + \left(\frac{d\Delta V}{dz}\right)^2\right)\mathbf{r}\mathbf{d}\mathbf{r}\mathbf{d}\Theta\right)}{\mathbf{A_{cr}}} = 0 \text{ at } 0 < z$$

$$< Z_1 u\rho_g Cp_g \frac{dT}{dz} - k_e \frac{d^2T}{dz^2} - \varepsilon \sum_j^{N_j} \left(-\Delta H_{rxn} R_{v,j}\right) - \frac{\left(\int_{r_1}^{r_2}\int_0^{2\pi} -\frac{1}{s_{bed}}\left(\left(\frac{d\Delta V}{dr}\right)^2 + \left(\frac{d\Delta V}{dz}\right)^2\right)\mathbf{r}\mathbf{d}\mathbf{r}\mathbf{d}\Theta\right)}{\mathbf{A_{cr}}} = 0 \text{ at } Z_1 < z < Z_2 \quad (8)$$

$$\Delta V = 0$$

$$\text{At } z = Z_2 \text{ and } r_1 \le r \le r_2$$

$$\frac{d\Delta V}{dz} = 0$$

$$\text{At } r = 0 \text{ and } 0 \le z \le Z_1$$

$$\frac{d\Delta V}{dr} = 0$$

where ΔV_{app} is the applied electric potential to the bed.

Once the 2D map of the electric potential was obtained, the electric field (E), current density (J), and linear Joule heating density field (dQ_{JH}) were determined using Eqs. (5) to (7), respectively, for a given bed resistivity. Because the electric field is perpendicular to surfaces of constant potential, current (equiflux) lines are orthogonal to equipotential lines. Equiflux lines satisfy boundary conditions inverted to the potential field: insulating surfaces become conductive, and conducting surfaces forbid normal current flow.

$$E_r = -\frac{d\Delta V}{dr},\ E_z = -\frac{d\Delta V}{dz} \quad (5)$$

$$J_r = -\frac{1}{s_{bed}}\frac{d\Delta V}{dr},\ J_z = -\frac{1}{s_{bed}}\frac{d\Delta V}{dz} \quad (6)$$

$$\frac{dQ_{JH,r}}{dz} = \int_0^{r_2}\int_0^{2\pi} -\frac{1}{s_{bed}}\left(\frac{d\Delta V}{dr}\right)^2 r\,dr\,d\Theta,\ \frac{dQ_{JH,z}}{dz} = \int_0^{r_2}\int_0^{2\pi} -\frac{1}{s_{bed}}\left(\frac{d\Delta V}{dz}\right)^2 r\,dr\,d\Theta \quad (7)$$

Eq. (4) was discretized using finite differences for a coaxial ETFB reactor with a conductive distributor, as shown in Fig. 1A. It was then solved using a custom-built Gauss-Seidel algorithm to analyze the field distribution of electrical properties within the reactor. The general Joule heating term ($dQ_{JH}\,dz^{-1}$) derived from the electric potential field using a Laplacian field model, for an ETFB reactor with the geometry depicted in Fig. 1A, was applied to Eq. (3) and presented in Eq. (8). In this configuration, r_1 and r_2 are the radius of the central electrode and the reactor

If the assumptions of constant s_{bed} and fixed expanded bed height H_{exp} are relaxed, the electrical problem changes in both mathematical structure and coupling requirements. If s_{bed} is evaluated from correlations (e.g., Fedorov et al. (Fedorov et al., 2016)) or allowed to vary with local temperature, porosity, or hydrodynamic conditions, the electrical problem assumes a variable-coefficient form, $\nabla\,(s_{bed}^{-1}(r,z)\,\nabla V) = 0$ which must be solved in full coupling with the heat and mass balances. Similarly, if the expanded bed height H_{exp} evolves with gas density, reaction extent, or solids holdup, the geometry of the electrical domain becomes operating-condition dependent, requiring recomputation of the potential field on a moving or updated domain at each iteration. In combination, spatially varying resistivity and variable bed expansion convert the Joule-heating calculation into a nonlinear multiphysics problem, substantially increasing mathematical complexity and computational cost and necessitating additional constitutive relations.

2.5.2. Current partition model

The detailed electric potential field in an ETFB reactor having a total bed height $H_{exp} = (Z_1 + Z_2)$ of 160 mm, a diameter (r_2) of 130 mm, central electrode diameter of 20 mm (r_1) and central electrode submersion of 100 mm (Z_2) is presented in Fig. 4 (left).

To better visualize and understand the regions where axial or radial current dominates, the contribution of the radial current density to the total current density magnitude ($\overline{\overline{J_r}} = \frac{J_r^2}{J_r^2+J_z^2}$) was plotted for the same central electrode dimensions, see Fig. 4 (right). The color scale indicates the relative contribution of the radial component, ranging from 0 (purely axial current flow, shown in blue) to 1 (purely radial current flow, shown in yellow). White contour lines illustrate the transition between different regions.

Based on this distribution, the system was divided into two main conductive zones. The first is the annular region around the central electrode, where the equipotential lines are vertical and the current flows primarily in the radial direction. This zone is conceptually represented by the Coaxial Resistor (CAR) in Fig. 4 (right). The second zone lies below the tip of the central electrode, where the equipotential lines are nearly horizontal, resulting in a predominantly axial current flow. This region is modeled as the Truncated Cone Resistor (TCR). Between these two regions is a transition zone, where the equipotential lines curve and the current exhibits both axial and radial components, this is

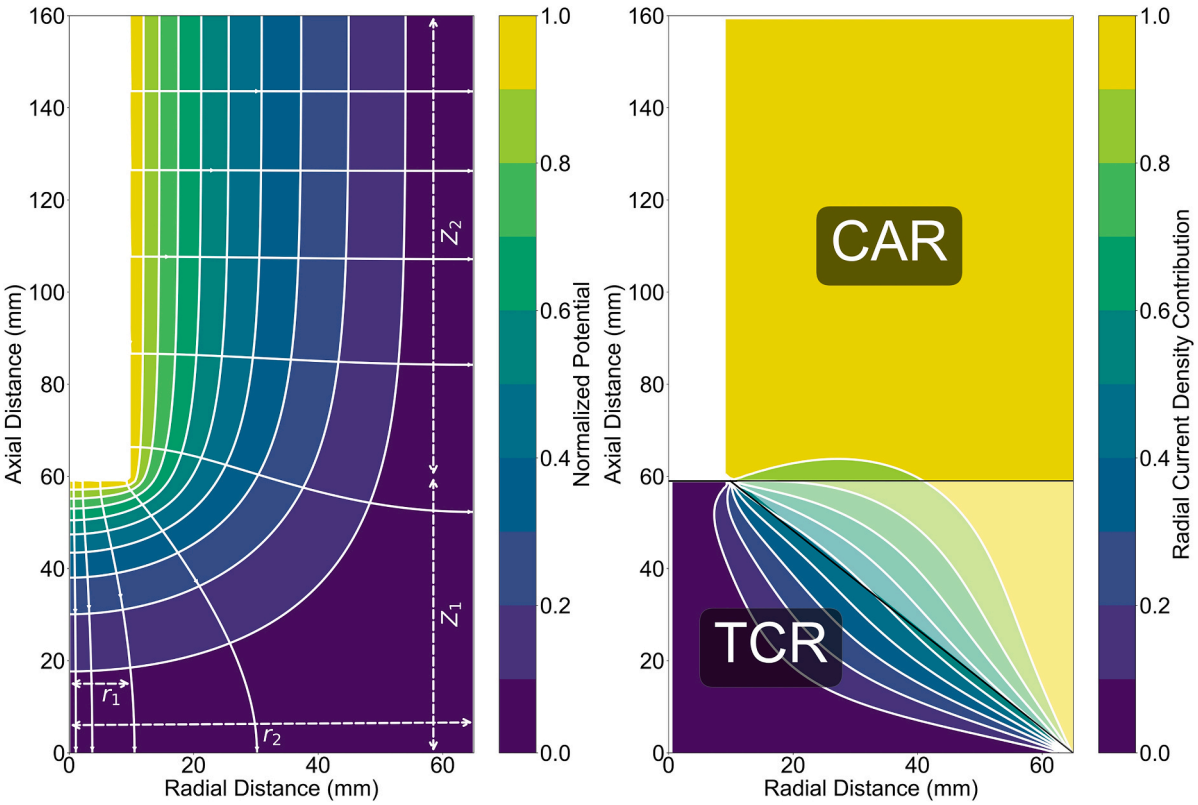

Fig. 4. Left: equipotential and equiflux lines in a coaxial ETFBR with conductive distributor. right: Conceptual current partition representation of electrical resistances in an coaxial ETFBR with conductive distributor: Coaxial (CAR) and Truncated Cone Resistors (TCR).

referred to as mixed current flow. Although this region was fully resolved in the 2D Laplacian field simulation, it poses a challenge for analytical modeling. The aim of this model is not to solve the 2D field explicitly, but rather to use it as a reference to construct a simplified yet physically meaningful model. In principle, the local Joule heating in a one-dimensional ETFB can be estimated using Eq. (7) which incorporate curvature effects. However, that would require solving the full multi-dimensional field for each configuration as stated in Eq. (8).

To avoid this complexity while still capturing the dominant conductive behavior, the system was approximated by partitioning it into two idealized resistive regions, one radial (CAR) and one axial (TCR). This allows for the use of analytical expressions tailored to each dominant direction without needing to explicitly resolve the intermediate curvature zone. Importantly, the CAR and TCR are conceptual constructs, not rigid physical boundaries. They represent the prevailing current paths in their respective regions and provide a structured framework for estimating Joule heating in a one-dimensional energy balance model. This formulation was not intended to represent the most optimal resistor geometry but rather to enable a structured analysis of the predominant current paths while avoiding the need for complex resistor geometries that would significantly increase computational cost and parameterization difficulty. It is acknowledged that part of the mixed current region is not explicitly accounted for, as the focus is on distinguishing the prevailing conductive zones to facilitate modeling

$$R = \frac{sL}{A_I} \tag{9}$$

By applying the definition of electrical resistance as expressed in Eq. (9), the differential resistance dR_{CAR} for radial current flow through a thin annular shell of thickness dr at a radial position r is given by Eq. (10). The cross-sectional area available for conduction at radius r is $A_I = 2\pi r Z_2$. The total resistance R_{CAR} is subsequently obtained by integrating over the radial domain from r_1 (the radius of the central electrode) to r_2 (the reactor wall), yielding the expression in Eq. (11). To extend this formulation, a height element Δz is introduced, segmenting the system into a finite number of coaxial resistors of height Δz. Since each of these resistors experiences the same potential difference ΔV, they are electrically configured in parallel. In the limit of an infinitesimally small height element, the resistance expression for a coaxial resistor was derived and presented in Eq. (12).

$$dR_{CAR,r} = \frac{s_{bed}dr}{A_I} \tag{10}$$

$$R_{CAR} = \frac{s_{bed}}{2\pi z_2}\mathrm{Ln}\left(\frac{r_2}{r_1}\right) = \left(\sum \frac{1}{\frac{s_{bed}}{2\pi\Delta z}\mathrm{Ln}\left(\frac{r_2}{r_1}\right)}\right)^{-1} \tag{11}$$

$$dR_{CAR} = \frac{s_{bed}}{2\pi dz_2}\mathrm{Ln}\left(\frac{r_2}{r_1}\right) \tag{12}$$

The differential resistance dR_{TCR} for axial current flow through a thin annular shell of thickness dz at an axial position z is given by Eq. (13). The cross-sectional area, $A_I = \pi r^2$, varies along the axial direction. Since the line connecting the tip of the central electrode to the bottom of the reactor is a straight line, the radius can be expressed as a function of the reactor length, as shown in Eq. (14). Substituting Eq. (14) into (13) and integrating over the axial length from $z = 0$ (bottom of the reactor) to $z = Z_1$ yielded the overall resistance of this section, as expressed in Eq. (15).

$$dR_{TCR} = \frac{s_{bed}dz}{\pi r^2} \tag{13}$$

$$r = -\frac{r_2 - r_1}{Z_1}z + r_2 \tag{14}$$

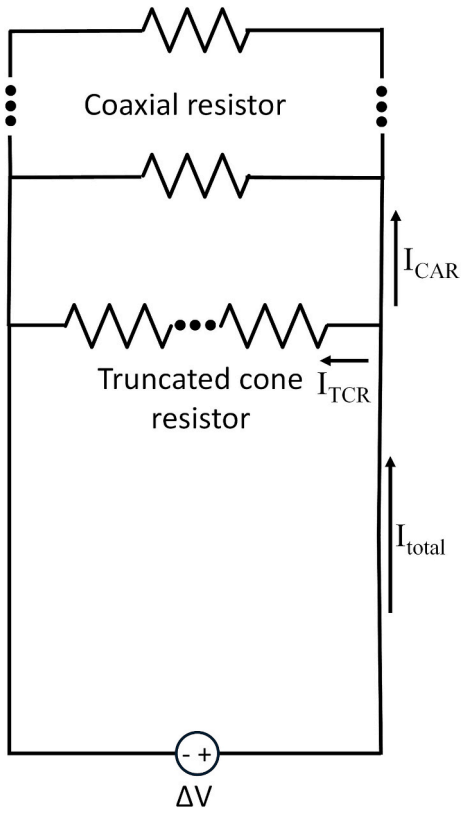

Fig. 5. The electrical characterization of the ETFB reactor as a circuit of mixed resistors based on current partition.

$$R_{TCR} = \frac{s_{bed} Z_1}{\pi r_1 r_2} = \sum \frac{s_{bed} \Delta z}{\pi r^2} \tag{15}$$

The electrical characteristics of the entire bed can be described as a combination of two conceptual resistors (TCR and CAR) in parallel with each other, as illustrated in Fig. 5. In this scheme, the coaxial resistor was treated as an array of infinitesimally small resistors in parallel, while the truncated cone resistor was represented by a series of infinitesimally small resistors. When an electrical potential is applied to the system, I is divided between I_{TCR} and I_{CAR}. This configuration forms the basis of a current partition model (CPM), where the total resistance of the bed can be determined through Eq. (16).

$$R_{bed} = \left(\frac{1}{R_{CAR}} + \frac{1}{R_{TCR}} \right)^{-1} \tag{16}$$

To derive the Joule heating term for each resistor, the equation for Joule heating, Eq. (17) was applied. For the coaxial resistor, the electric potential remained constant along the axial direction. Consequently, the Joule heating generated over an infinitesimal height element dz was obtained by substituting Eq. (12) into (17). The resulting expression for the heat produced in a height element of the coaxial resistor, $dQ_{JH,CAR}$, is presented in Eq. (18). Similarly, for the truncated conical resistor, substituting Eq. (13) into (17) yields the expression for the heat generated in a height element, $dQ_{JH,TCR}$, as shown in Eq. (19).

$$Q_{JH} = I^2 R = \frac{\Delta V^2}{R} \tag{17}$$

$$\frac{dQ_{JH,CAR}}{dz} = \frac{\Delta V^2 2\pi}{s_{bed} \ln\left(\frac{r_2}{r_1}\right)} \tag{18}$$

$$\frac{dQ_{JH,TCR}}{dz} = \frac{I_{TCR}^2 s_{bed}}{\pi r^2} \tag{19}$$

After deriving the Joule heating terms for each resistor, Eqs. (18) and (19), the final step was to substitute the expressions based on the current partition model into Eq. (3). This resulted in a single overall heat balance for the ETFB reactor that incorporates Joule heating as a function of the applied voltage and current, as shown in Eq. (20).

$$u\rho_g Cp_g \frac{dT}{dz} - k_e \frac{d^2T}{dz^2} - \varepsilon \sum_j^{N_j} \left(-\Delta H_{rxn} R_{v,j} \right) - \frac{I_{TCR}^2 s_{bed}}{\pi r^2 A_{cr}} = 0 \text{ at } 0 < z < Z_1 u\rho_g Cp_g \frac{dT}{dz} - k_e \frac{d^2T}{dz^2} - \varepsilon \sum_j^{N_j} \left(-\Delta H_{rxn} R_{v,j} \right) - \frac{\Delta V^2 2\pi}{s_{bed} \ln\left(\frac{r_2}{r_1}\right) A_{cr}} = 0 \text{ at } Z_1 < z < Z_2 \tag{20}$$

In constant-voltage operation, I_{TCR}, follows directly from Ohm's law once the CAR–TCR resistance network is known. When s_{bed} is prescribed, this resistance can be evaluated analytically. However, if s_{bed} depends on temperature, gas composition, porosity, or conversion, the resistance of the TCR cannot be established beforehand. In such cases, an initial guess for the TCR resistance is required, and the resulting current must be recomputed as part of the outer iterative loop that updates the reactor thermodynamic and hydrodynamic state. Specifically, after each solution of the coupled mass and heat balances, the average bed temperature T_{avg}, gas composition, and hydrodynamic descriptors are updated. If s_{bed} is a function of these quantities, even if it assumed to be constant throughout the bed, it must also be recalculated at each outer iteration. The updated resistivity modifies the CAR–TCR resistance network, which in turn alters I_{TCR}, the local Joule-heating rate, and thus the subsequent temperature field. In this way, the CPM becomes directly coupled to the reactor-scale solution procedure, with electrical quantities updated with thermal and compositional variables.

In constant-current operation, the imposed total current I_{total} is fixed, and the voltage drop ΔV follows from the circuit in Fig. 5. Yet the same coupling applies: if s_{bed} is not prescribed but evaluated from average properties, the CAR–TCR resistance and resulting ΔV must be recalculated at every outer iteration.

3. Electrothermal behaviour and design implications

The LFM and the CPM describe the same underlying physical phenomenon, electric potential distribution and Joule heat generation inside an ETFB reactor, but at fundamentally different levels of spatial resolution. The LFM solves the two-dimensional Laplace equation, fully resolving geometric field distortions, curvature of equipotential lines, and the resulting non-uniform current density distribution. In contrast, the CPM represents the bed as a network of equivalent resistive segments, partitioning the total current into radial and axial components using analytical expressions derived from the reactor geometry and an assumed uniform resistivity.

As such, the CPM functions as a reduced-order derivation of the LFM: it preserves the dominant current-partitioning mechanisms but neglects local variations and field curvature captured by the full Laplacian solution. Agreement between the two models is expected when current flow is primarily axial and geometric distortions are mild (e.g., deep or slender electrodes), whereas discrepancies are expected in cases where radial current redistribution is strong (e.g., shallow or wide electrodes). Understanding this relationship provides the conceptual grounding necessary for interpreting the quantitative comparison between the two modelling approaches.

The analysis presented in this section examines how reactor geometry and electrode configuration influence the spatial distribution of Joule heating and the resulting thermal and reactive behavior of the bed. These results highlight physically interpretable trends that can inform

the selection of electrode dimensions and bed geometry for targeted operating conditions, while avoiding claims of optimal design or validated operating limits.

3.1. Comparison of Laplacian field and current partition models

Building on this conceptual relationship, a systematic comparison between the predictions of the more detailed, field-resolved LFM and the analytically simplified CPM was conducted to assess the impact of model simplifications on accuracy. More specifically, this comparison evaluates whether the partition-based approach can capture key electrical outputs (Q_{JH} and $dQ_{JH}\,dz^{-1}$) without significant deviation from the more detailed field-based model. This analysis provides insight into the trade-off between computational efficiency and model fidelity, helping to validate the applicability of the simplified methodology. For this comparison, the reactor geometry was fixed with a bed height of 160 mm, a diameter (r_2) of 130 mm, and an applied electric potential of 20 V. To systematically evaluate the differences between the two approaches, the electrode submersion depth and diameter were varied across a wide range of possible values.

3.1.1. Deviation of CPM from LFM across electrode geometries

The deviation maps in Fig. 6 to Fig. 8 provide a fully quantitative comparison between the two models across the entire geometric parameter space. Each point in these maps represents the percentage error between the CPM and LFM predictions, allowing direct assessment of both the magnitude and spatial structure of the model deviation. The following discussion highlights the dominant quantitative trends extracted from these data. The colour map represents the percentage deviation in power prediction between the two models, as defined in Eq. (21), where k corresponds to total Joule heating (tot), Joule heating due to radial current (r), and Joule heating due to axial current (z). The x-axis represents the ratio of the electrode's radius to the reactor's radius while the y-axis represents the electrode's submersion depth as a fraction of the total bed height. Red regions indicate positive deviations, where the current partition model predicts more Joule heating than the LFM while blue regions represent negative deviations.

$$\xi_{,k} = \left(\frac{Q_{CPM,k} - Q_{LFM,k}}{Q_{CPM,k}}\right) \times 100 \tag{21}$$

The comparison between the two models identifies a central region of the design space where the total power predicted by the CPM deviates by no more than ± 20% from the LFM within the region that corresponds to electrode widths between 10% and 90% of the reactor radius and submersion depths between 20% and 80% of the total bed height. Within this range, the CPM provides an approximate representation of Joule heating trends, though deviations are not always negligible. Notably, deviations between the models remain relatively stable across electrode widths, suggesting that the CPM captures the radial distribution of current with reasonable consistency. In contrast, deviations become more pronounced at very shallow or deep submersion depths. At low submersion, the annular current path is underdeveloped, leading to underprediction of Joule heating. At high submersion, strong axial field gradients beneath the electrode tip are not well captured by the CPM, resulting in overprediction. These discrepancies stem from the CPM's geometric simplifications and its inability to resolve electric field curvature, an effect explicitly captured by the LFM.

Importantly, the largest deviations occur in configurations that are physically unrealistic or operationally undesirable. Extremely shallow submersions suppress radial heating altogether, while very deep submersions shift the heating zone below the active region of the bed. These cases are typically avoided in practical reactor designs, reinforcing that the CPM can be used within a meaningful subset of the design space, but with limited reliability near geometric extremes. Although electrode width has less influence on model deviation, it remains a critical design parameter. Narrow electrodes increase resistance due to longer current paths, while wider electrodes reduce electrical resistance but reduce the bed volume available for gas–solid interactions. These trade-offs should be considered during system-level design, even if they have limited impact on CPM accuracy.

The LFM is particularly advantageous for quantitative applications such as techno-economic analysis (TEA), life cycle assessment (LCA), and reactor optimization, where accurate prediction of power input and spatial energy deposition is essential. By fully resolving the electric field, it allows reliable estimation of localized heating, field gradients, and energy coupling to reaction zones. Conversely, the CPM may serve as a

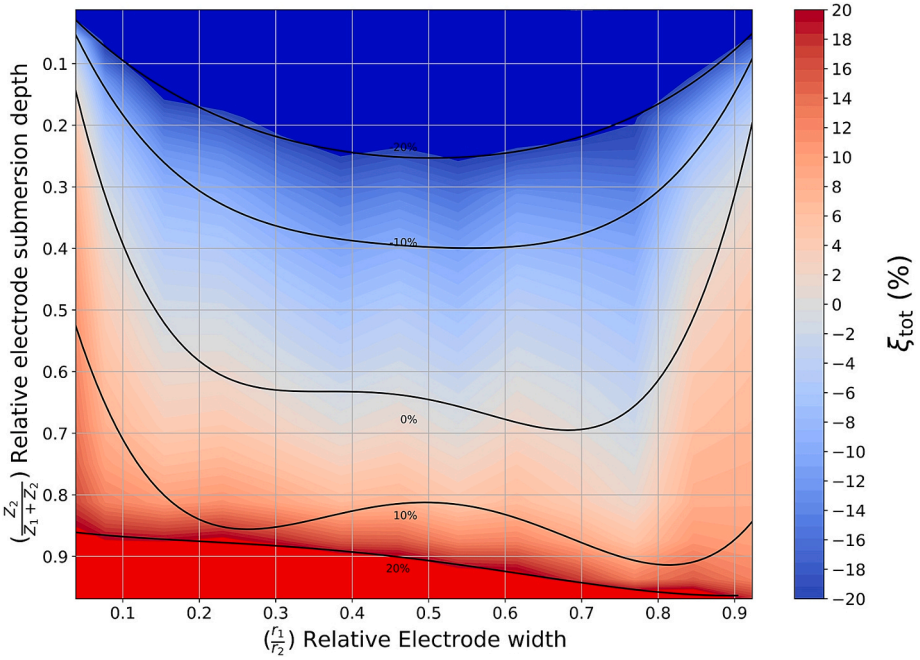

Fig. 6. Relative deviation between the total power predicted by the Current Partition Model and the Laplacian Field Model.

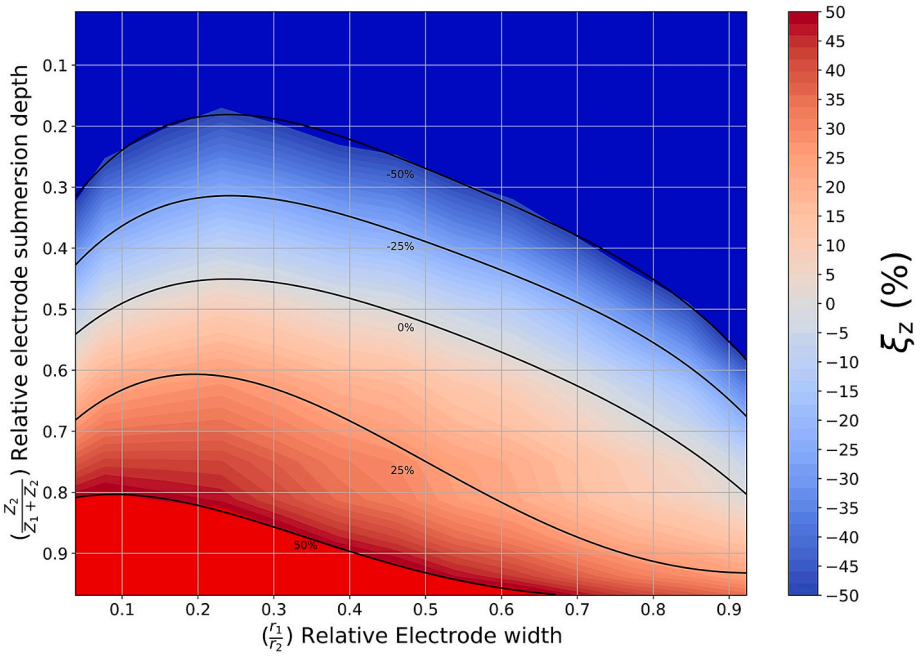

Fig. 7. Relative deviation between the Current Partition Model and the Laplacian Field Model for Joule heating caused by the axial current component.

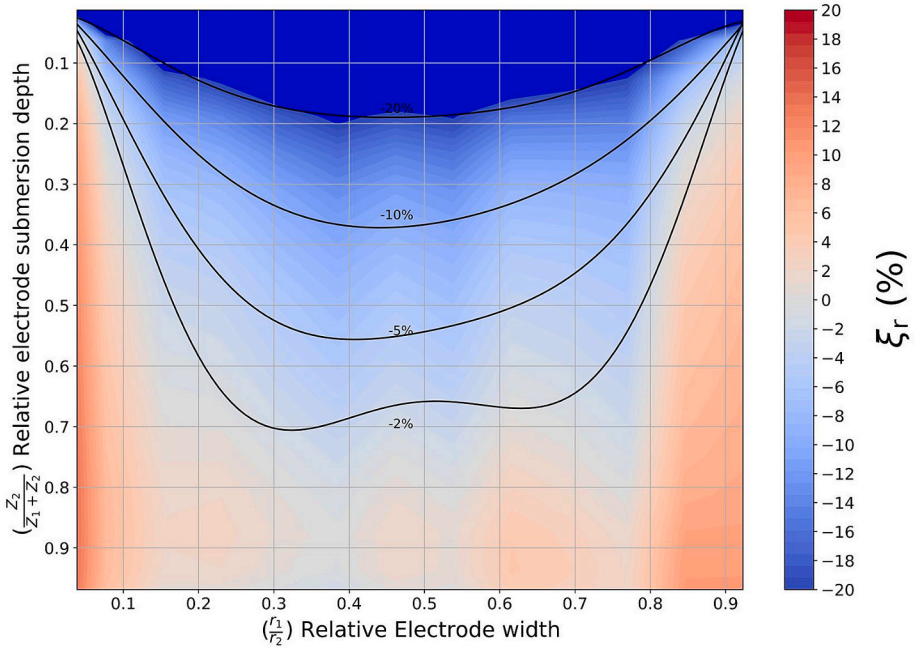

Fig. 8. Relative deviation between the Current Partition Model and the Laplacian Field Model for Joule heating caused by the radial current component.

useful tool for qualitative assessment, conceptual screening, or early-stage design studies where computational efficiency is prioritized and some loss in spatial resolution is acceptable. The selection of a modeling approach should ultimately depend on the required precision and the sensitivity of the application to electric field distribution.

To better understand why the electrode submersion depth has a greater effect on the deviation from the LFM, a comparative analysis was conducted by isolating the contributions of radial and axial current flow. Specifically, the Joule heating predictions from the current partition model and the LFM were compared separately for the Joule heating produced only due to axial current flow (Fig. 7) and radial current flow (Fig. 8) approach allows for a more detailed assessment of how each current component contributes to the overall deviation and provides insight into the dominant factors affecting the accuracy of the current partition approximation.

The deviation in Joule heating due to the axial current component exhibits a distinct trend, with significantly larger deviations compared to the Joule heating contribution from radial current. For submersion depths exceeding 80% of the total bed height and narrow electrodes occupying less than 20% of the reactor radius, the CPM predicts axial Joule heating values that exceed the LFM values by more than 50%. This overestimation occurs because the partition model assumes a purely axial current path below the electrode tip, neglecting significant radial current redistribution into the surrounding bed, which is captured in the

LFM. As the central electrode widens, the electric potential gradients around the electrode tip intensify, increasing local axial effects and reducing radial current contributions. This reduces the discrepancy between the CPM and LFM, particularly for the axial component. While the axial current region does elongate with increasing submersion depth, raising the total resistance, the degree of current confinement and directional dominance is also enhanced, slightly improving the CPM's alignment with the LFM. Nonetheless, this does not fully eliminate the model's limitations, and large overestimations persist in geometrically extreme cases. This further reinforces the importance of interpreting CPM predictions with caution in such configurations.

Conversely, when the electrode submersion depth decreases below 40% of the bed height and the electrode becomes narrower than 30% of the reactor radius, a more prominent mixed-current region emerges below the electrode tip, where axial and radial currents interact more strongly. The current partition model fails to account for this effect, leading to a significant underestimation of Joule heating due to the axial current component.

Thus, the field model more accurately captures the interplay of radial and axial currents, while the current partition model provides a simplified approximation that overestimates axial Joule heating at large submersion depths and underestimates it at shallower depths and narrower electrodes.

This behavior highlights the limitations of the truncated cone resistor restriction in capturing the complexity of axial current flow, particularly in the transition region where the current distribution deviates from the assumed discrete axial-to-radial separation. The stronger dependence of the axial contribution on electrode radius suggests that axial current pathways are more sensitive to variations in electric field distribution, which the current partition model does not fully account for.

Furthermore, the overestimation of power generation at high submersion depths may be attributed to the assumption that all current transitions into axial flow within a well-defined region, whereas the LFM indicates a more gradual transition with significant mixed-direction currents. Conversely, at low submersion depths, the current partition model likely underestimates Joule heating due to an oversimplification of how current distributes near the electrode tip.

Rather than aiming to determine the most optimal resistor configuration or geometry, this work provides a systematic approach to simplify the complex phenomenon of Joule heating in an ETFB reactor. By formulating the problem in terms of fundamental electrical concepts, i.e., electric potential and current, it offers a practical framework for understanding the system while preserving its physical essence. This approach enables a clear comparison between different modeling strategies, highlighting the strengths and limitations of the current partition model while maintaining physical relevance in reactor design considerations. The LFM, though computationally more demanding, remains the most reliable reference framework for evaluating electric field behavior and resistive heating under arbitrary electrode configurations. As such, it forms the physical and conceptual foundation upon which all further simplifications must be validated.

Although the deviation maps presented here correspond to a specific electrode configuration, the comparison methodology itself is general. The same quantitative framework can be applied to other reactor and electrode geometries by imposing the appropriate electrical boundary conditions in the Laplacian Field Model and constructing the corresponding equivalent resistor network in the Current Partition Model.

3.1.2. *Effect of central electrode submersion depth on power density profile and total Joule heating*

The LFM is the primary framework in this study. It delivers a geometry-resolved, continuous field and current distribution for the specified electrode layout and boundary conditions, and its linear power-density profiles (Fig. 9, left) set the reference physical picture. In parallel, the CPM is used as a reduced-order, analytical complement for rapid evaluation; comparisons to the LFM are reported to clarify the scope of its simplifications and their impact on predictions.

The linear power density predicted by the LFM (Fig. 9, left) exhibits a distinct behavior in the region around the tip of the central electrode. This divergence from the current partition approach arises because the LFM employs a continuous representation of the current, as opposed to the partition based approximation. In this framework, while axial or radial current may dominate in different spatial regions, both components are present throughout the entire bed volume, contributing to the overall Joule heating distribution. Moreover, the LFM inherently captures the curvature of the electric potential field surrounding the electrode tip (see Fig. 4, left), a feature that is not as readily represented in partition based models.

As a consequence of these characteristics, the region beneath the electrode tip experiences a gradual, quadratic increase in linear power density, culminating in a peak whose magnitude and position are governed by two primary factors: the submersion depth of the electrode and the intensity of the applied electric field. Specifically, as the central electrode is submerged deeper into the bed, the location of this peak shifts further downward within the reactor, while its magnitude increases. This behavior is attributed to the corresponding increase in electric potential gradients in the lower region of the bed, which enhances localized Joule heating.

A key implication of the current partition model, assuming constant resistivity, is that the linear power density (power per unit length, kW m^{-1}) remains uniform within the CAR and increases quadratically within the TCR, as shown in Fig. 9 (right) In the CAR, the linear power density is independent of the central electrode's submersion depth. This is because the characteristic length of this region, i.e., the distance between the vertical surface of the central electrode and the reactor wall, remains constant, regardless of the electrode's depth of submersion. However, although the linear power density remains constant, the total power increases with a deeper electrode submersion due to the larger

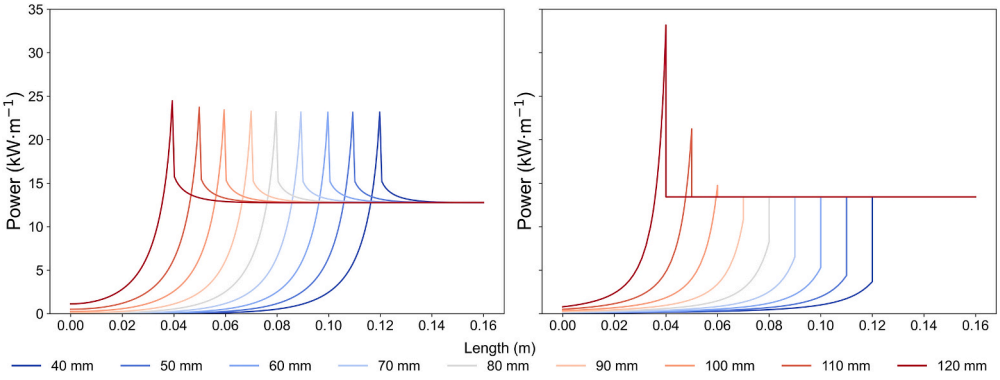

Fig. 9. Linear power density profile. left: Laplacian Field Model. right: Current Partition Model.

central electrode bed exposure.

In contrast, in the TCR, the linear power density increases quadratically along the length of the reactor, particularly towards the tip of the electrode. As the electrode submersion depth increases, the magnitude of the power density also increases. The characteristic length of the TCR is defined as the distance between the tip of the central electrode and the distributor, which decreases as the electrode is submerged further into the bed. Consequently, the length over which the current flows radially decreases, resulting in a decrease in the resistance of the system. This reduction in resistance leads to higher Joule heating in this region.

A distinguishing feature of the current partition model is the absence of a transitional region between the CAR and the TCR. At the tip of the electrode, the linear power density shifts abruptly from a constant value in the CAR to a quadratically increasing profile in the TCR. This discontinuity is a result of the modeling simplification, which assumes distinct and non-overlapping resistive zones. As a consequence, a small segment of the bed around the electrode tip where in reality both axial and radial currents are present is not explicitly accounted for. In the simplified representation, this zone appears as a 'gap' or abrupt transition in the power profile (see Fig. 9, right).

The TCR explicitly defines a conical geometry with a fixed, decreasing cross-sectional area, leading to a strictly geometric quadratic increase in power density along the cone's length. In the LFM, however, no physical cone occurs; instead, the quadratic increase in power density arises naturally due to the curvature of equipotential lines and the natural development of axial current flow below the electrode tip according to the field equations, Eq. (7). Unlike the current partition model, where power density transitions discontinuously from the TCR to the CAR region, the LFM predicts a smooth and continuous transition, driven by the interplay between radial and axial current components rather than an imposed resistor partition. This distinction highlights the fundamental difference in how each model conceptualizes Joule heating: one as a function of imposed resistor regions, the other as an emergent result of electrostatic potential distribution.

It is important to acknowledge that the assumption of constant resistivity introduces some limitations in predicting the exact power distribution, as resistivity is generally temperature-dependent. Joule heating affects temperature, and the temperature in turn influences electrical conductivity. A fully coupled approach that accounts for temperature-dependent resistivity would provide a more accurate prediction of the power distribution, as the dynamic interplay between temperature and resistivity would be better represented. Despite this limitation, the general trends predicted by the current partition model are consistent with physical principles and align well with expectations based on theoretical understanding.

The trends observed in the linear power density are also evident when analyzing the total Joule heating predicted by both models (Fig. 10). The total power in both the CPM and the LFM increases as the central electrode is submerged deeper into the bed. This aligns with the understanding that a deeper electrode submersion expands the conductive surface area available for radial current flow, thereby reducing overall resistance and increasing total Joule heating. The total power predicted by the CPM and the LFM exhibit a similar evolution, demonstrating a consistent increase with decreasing ESD (electrode submersion depth), from 1.81 kW at 120 mm to 0.60 kW at 40 mm (CPM) and from 1.74 kW at 120 mm to 0.70 kW at 40 mm (LFM). This consistency underscores the fundamental role of submersion depth in dictating the extent of Joule heating in the system. Overall, the total power trends reinforce the conceptual distinctions between the two models. The increasing total power with deeper submersion, the dominance of radial current, and the differences in predicted power distributions all align with the theoretical framework established for linear power density. At the same time, the observed shift from underprediction to overprediction by the CPM highlights the strengths and limitations of each model, further emphasizing the impact of current partitioning assumptions on Joule heating predictions.

3.2. Thermal model validation

To evaluate the predictive capability of the proposed thermal model, its predictions are compared with reported operating data for a real ETFB from the literature (Ahmed et al., 2025). The experimental dataset comprises steady-state measurements of applied voltage, total electrical power, and bed temperature for different electrode submersion depths. Because the reported experiments were performed under non-reactive argon heating conditions, this validation focuses on the electrothermal and heat-transfer components of the framework. In the assessment, all modelling assumptions established in Section 2 are retained. In addition,

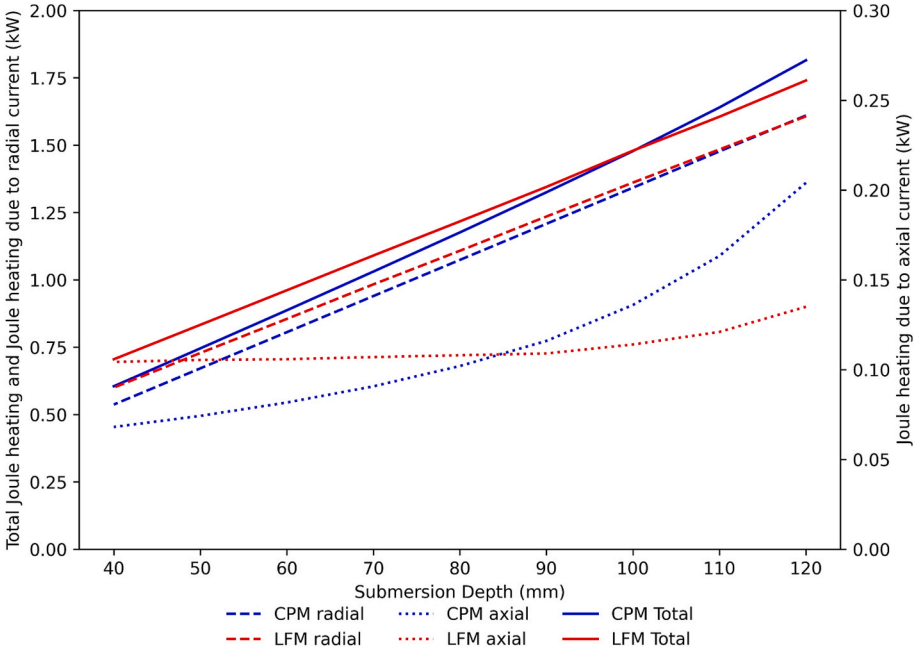

Fig. 10. Joule heating from radial and axial currents, and total heating, as predicted by the Current Partition Model (CPM) and Laplacian Field Model (LFM). V = 20 V, s_{bed} = 10 Ω cm.

the idealized adiabatic heat balance is extended to account for heat losses through the insulation as well as to include an adjusted top boundary condition accounting for both convective and radiative losses. Consistent with the experimental setup, the initial (pre-fluidization) bed height was 130 mm for all cases. This value was adopted as H_{exp} in order to maintain consistency with the fixed H_{exp} assumption used throughout the reactor-scale model. The jumbo particle case (d_p = 338 μm) was selected for analysis, as it provides the most complete and consistent set of operating points across electrode depths and temperatures, making it the most suitable reference for an initial thermal model assessment. Only operating points with reported temperatures above 600 °C were considered. Furthermore, the authors report that the thermocouple is aligned with the bottom edge of the central electrode; accordingly, model–data comparisons were performed using the predicted temperature at the electrode tip, i.e. T(z = Z_1). Because neither the outer diameter of the ETFB and the thermal conditions in the freeboard region were reported, the insulation outer radius was assumed as $r_o = 2r_2$, and the overhead reference temperature was set to 200 °C for all cases. The extracted data and the adapted governing expressions are provided in the Supplementary Information.

As s_{bed} is an input to the reactor-scale framework, an estimate of this value is required for the literature cases. To obtain such an estimate, an additional simplifying assumption was made, namely, that the reported electrical power is fully dissipated within the bed volume as Joule heating, neglecting any potential electrical losses outside the bed phase, such as line losses and contact resistances at the electrode surfaces. Under these assumptions, s_{bed} was estimated using the LFM electrical model by adjusting its value such that the computed total Joule power matches the reported power for each operating point. When the resulting values are grouped by immersion depth of the central electrode (ICE, following the authors' nomenclature), average resistivities of approximately 12.94 Ω.cm (ICE = 25 mm), 15.22 Ω.cm (ICE = 60 mm), and 23.44 Ω.cm (ICE = 95 mm) are obtained. This trend is consistent with the authors' observation that the effective bed resistivity s_{bed} grows with increasing ICE.

Using the extracted experimental voltages together with the estimated s_{bed} values, the thermal model was applied to predict the temperature at the electrode tip location. Because the dominant thermal loss mechanisms in the reactor are governed primarily by the available heat-transfer area rather than by case-specific operating conditions, a robust reactor-scale description should be able to reproduce the experimental trends using a minimal set of effective heat-transfer parameters. Therefore, the wall losses were represented through a single overall radial heat transfer coefficient, h_{tot}, while the top boundary losses were captured using a single convective coefficient, h_{top}, with the granular graphite emissivity assumed as 0.85. To account for uncertainty associated with manual data extraction from published figures as well as variability in the reported experimental measurements, the electrical inputs (V_{app}, s_{bed}) were allowed to vary within ± 1% of their nominal values. For each ICE, a single pair of parameters (h_{tot}, h_{top}) was identified across all corresponding operating points.

The parity diagrams in Fig. 11 summarize the agreement between experimentally reported and predicted electrode-tip. The LFM predictions (Fig. 11, Left), reproduce the overall experimental temperature trends well across all electrode immersion depths, with all of the operating points lying within the ± 50 °C band. The CPM predictions (Fig. 11, Right), evaluated using the same electrical and thermal inputs, show comparable agreement for ICE = 60 and 95 mm, supporting the suitability of the CPM as a reduced-order approximation for reactor-scale thermal modelling. Consistent with the deviations observed earlier in Fig. 6, the CPM tends to underpredict Joule heating at shallow electrode submersion, which explains why the ICE = 25 mm cases fall systematically below the − 50 °C band. Overall, the parity diagrams demonstrate that the proposed electrothermal framework is capable of reproducing reported ETFB temperature trends across electrode immersion depths using a minimal and physically interpretable set of parameters. The close agreement obtained with the field-resolved LFM confirms the internal consistency of the formulation in linking electrical inputs, Joule heating, and thermal response at the reactor scale. The simplified CPM yields comparable agreement for intermediate and deep electrode immersion depths, consistent with its reduced-order nature and the deviations identified earlier for shallow submersion. Together, these results show that the governing electrothermal formulation captures the dominant reactor-scale behavior while clarifying the range of applicability of each modelling strategy. Detailed results and relevant model parameters for all simulations, together with a more in-depth analysis and interpretation of the results, are provided in the Supplementary Information.

3.3. Application of the electrothermal modeling strategies to a reactive system

To evaluate the behavior of the electrothermal fluidized bed reactor under strongly heat-demanding conditions, the modelling framework

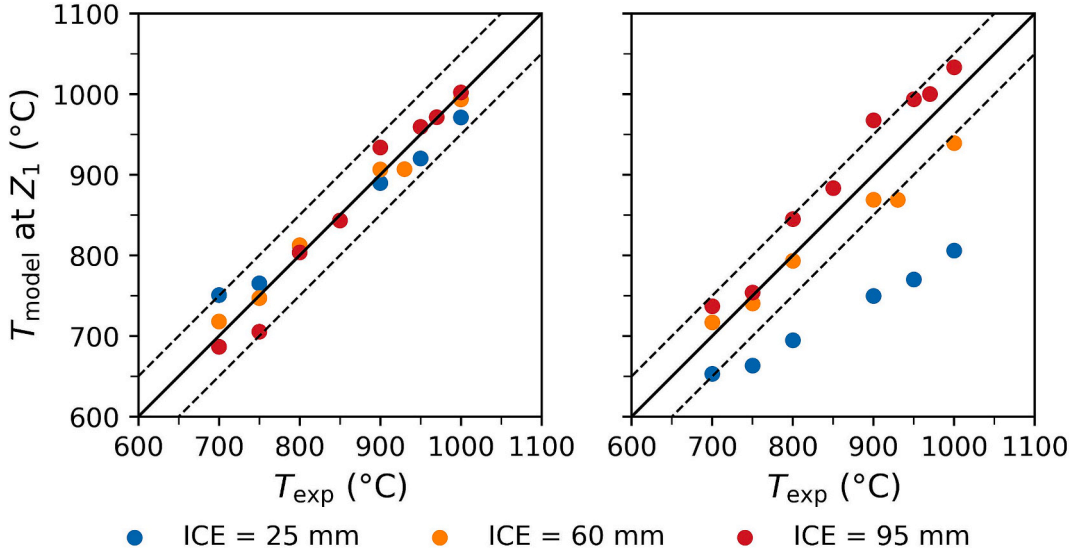

Fig. 11. Parity diagram of experimental and predicted electrode-tip temperatures for different ICE values. Left: predictions obtained with the LFM. Right: predictions obtained with the CPM using identical electrical and thermal inputs.. Dashed lines denote ± 50 °C error.

was applied to the thermal decomposition of carbonyl sulfide (COS). This reaction forms the second step of the process targeted in the e-CODUCT project and has already been outlined in the introduction. It operates at high temperatures and is highly endothermic, making it an appropriate benchmark for assessing the reactor's ability to supply distributed Joule heating under reactive operation. The kinetic expressions and thermochemical data used in this study are provided in the Supplementary Information. In this context, COS conversion is used as a qualitative design metric, and a target conversion level of approximately 90% is adopted as an illustrative benchmark rather than an operational specification.

The purpose of this case study is not to validate the kinetics, nor to represent the full e-CODUCT flowsheet, but rather to examine how the electrothermal model performs when conversion, heat demand, and temperature are simultaneously coupled.

It should be noted that, unlike the preceding model assessment against experimental ETFB reference data (Section 3.2), the present reactive simulations are performed using the idealized adiabatic heat-balance formulation introduced in Section 2.3. Heat losses through insulation and the top boundary are therefore neglected in this case study, allowing the intrinsic coupling between Joule heating, temperature evolution, and endothermic reaction demand to be examined under controlled reactor-scale assumptions.

In the present reactor-scale formulation, no direct coupling exists between the electric potential field and the hydrodynamic field. The power-density field depends only on geometry and electrical boundary conditions and is therefore independent of local temperature, gas composition, or fluidization state. The electric field influences the reactor solely through the spatial distribution of volumetric Joule heating.

Because of this one-way coupling, the electric potential field is solved only once for each electrode configuration using the Laplacian Field Model or the Current Partition Model. The resulting axial Joule-heating density profiles (Fig. 9) are then supplied as fixed inputs to the reactor heat balance during the reactive simulations. Temperature changes arising from this heating modify the gas density and thermophysical properties, which in turn affect the superficial velocity and residence time. Thus, variations in geometric or electrical parameters, such as electrode submersion depth, affect hydrodynamic quantities indirectly through thermal effects rather than through any electrohydrodynamic mechanism. This indirect thermal–hydrodynamic coupling becomes especially relevant under reactive conditions, where strong endothermicity amplifies the competition between heat generation and heat consumption.

To directly compare the electrical results of the LFM and the CPM, the bed dimensions are kept consistent with those used in section 3.1. Specifically, the reactor maintains a fixed diameter of 130 mm and a height of 160 mm. The central electrode diameter is also fixed at 20 mm within the ETFB reactor for this case study. However, the electrode submersion depth is varied between 40 mm and 120 mm, corresponding to a predicted deviation in total power of − 16% to + 4% respectively with respect to the LFM to examine how these differences influence the resulting temperature and conversion profiles within the reactor. For all simulations.. the feed consists of 2 kg h^{-1} of a 50% COS/N_2 mixture at atmospheric pressure. The temperature of the feed just below z = 0 is maintained at 600 °C. Particle diameter and particle density are assumed to be 100 μm and 2000 kg m^{-3} respectively for all cases. Particle heat capacity correlation (Butland and Maddison, 1973) can be found in supplementary information.

3.3.1. Effect of electrode submersion depth on thermophysical and bed parameters

Table 1 presents the effect of increasing electrode submersion depth on key thermophysical and bed parameters for the simulations using the current partition model. The results highlight the strong coupling between temperature, hydrodynamics, and transport phenomena in the system.

Table 1
Effect of changing the central electrode submersion depth on thermophysical and bed parameters.

	Electrode Submersion depth		
Parameter	40 mm	120 mm	unit
t_r	4,9	3,8	s
u	0,10	0,13	m s^{-1}
Cp_g	1,065	1,068	kJ kg^{-1} K^{-1}
μ_g	3,5 x 10^{-5}	3,9 x 10^{-5}	Pa s
K_g	5,9 x 10^{-5}	6,9 x 10^{-5}	kW m^{-1} K^{-1}
ρ_g	0,58	0,46	kg m^{-3}
u_{mf}	6,5 x 10^{-3}	6,5 x 10^{-3}	m s^{-1}
Ar	9,45	5,97	–
u_{cr}	1,14	1,3	m s^{-1}
d_b	0,024	0,029	m
ε_{mf}	0,46	0,46	–
ε	0,57	0,60	–
Ψ_L	0,22	0,26	–
q_L	0,95	0,96	–
u_L	0,43	0,49	m s^{-1}
D_L	4,0 x 10^{-3}	5,7 x 10^{-3}	m^2 s^{-1}
D_H	9,8 x 10^{-3}	1,5 x 10^{-2}	m^2 s^{-1}
k_{LH}	0,42	0,49	m s^{-1}
k_e	4,4 x 10^{-2}	5,9 x 10^{-2}	kW m^{-1} K^{-1}

As the electrode is submerged deeper, t_r decreases from 4.9 s to 3.8 s, while u increases from 0.10 to 0.13 m s^{-1}. Both parameters are evaluated at average bed conditions and reflect the gas expansion caused by the temperature increase and reaction progress. The reduction in residence time directly impacts reaction progress, while the increased superficial velocity enhances particle motion and mixing.

Ar number, which is a dimensionless number used in fluid mechanics to characterize the relative influence of buoyancy and viscous forces, decreases from 9.47 to 5.97 upon deeper submersion, demonstrating how higher temperatures reduce ρ_g while increasing μ_g. This shift in properties weakens inertial forces and enhances viscous effects, which could lead to a transition toward smoother fluidization. Consequently, d_b increases together with u_L. At the same time, ε increases, signifying a more expanded and dispersed bed structure.

The higher porosity also leads to an increase in Ψ_L and q_L. This suggests that a greater proportion of the gas bypasses the dense phase, which can impact mass transfer and reaction performance.

Additionally, the mixing parameters increase with submersion depth. The axial dispersion coefficients of both phases rise, reflecting enhanced axial mixing due to higher turbulence and bubble motion. Both phases show similar relative increases, though D_H remains consistently higher in magnitude, making dispersion in the emulsion phase the dominant mechanism of axial mixing in the bed. As reported in Table 1, the dispersion coefficients are well above typical molecular diffusivities for binary gases at similar temperatures (Walker and Westenberg, 1960), confirming the convective dominance of mixing in this regime. The interphase mass-transfer coefficient and the effective thermal conductivity also rise with submersion depth, indicating stronger bubble–emulsion exchange and more efficient heat spreading throughout the bed. These bulk trends arise from the combined effects of higher temperature, gas expansion, and increased superficial velocity at deeper electrode positions. The present model is designed to capture reactor-scale behavior; while local mixing variations close to electrode surfaces are not resolved, they remain relevant for detailed fluidization studies and could be investigated with specific CFD simulations. While both the superficial velocity and Archimedes number remain far from the transition from the bubbling to the turbulent regime, since u_{cr} is still much higher than u and *Ar* remains above 1, it is crucial to consider these potential hydrodynamic changes when designing an ETFB reactor. The results show that electrode submersion depth impacts bed hydrodynamics, which, in turn, can affect the mechanisms of electrical current transfer in beds of electrically conductive particles. As a result,

optimizing electrode placement is essential not only for effective heating but also for maintaining stable fluidization and ensuring proper electrical conduction pathways within the bed. Notably, while the absolute values differ slightly, simulations using the Laplacian field model exhibit the same overall trends, further reinforcing the robustness of these observations across different modeling approaches.

3.3.2. *Effect of electrode submersion depth on temperature and conversion profiles*

Fig. 12 shows the effect of the central electrode submersion depth on temperature, while Fig. 13 illustrates its effect on COS decomposition conversion. In the CPM (Fig. 12 and Fig. 13, right), increasing the electrode submersion depth induces an increase in T_{avg} from 770 °C at 40 mm to 1007 °C at 120 mm. Higher temperatures accelerate reaction rates, promoting faster and more complete COS conversion along the reactor length. Upon deeper submersion, the conversion rises sharply and reaches a higher final value (90% at 120 mm). In contrast, for shallower depths, the reaction is more kinetically limited, leading to a lower conversion and a lower final value (54% at 40 mm).

For the LFM (Fig. 12 and Fig. 13, left), at a 40 mm submersion depth, the predicted average bed temperature is 796 °C, compared to 770 °C in the partition model, resulting in COS conversions of 61% and 54%, respectively. This trend continues up to a submersion depth of 100 mm. However, upon deeper submersion, the difference in conversion between the two models diminishes due to reaction kinetics. At 80 mm, despite a 15 °C difference in average temperature, conversion differs by just 1 percentage point (80% vs. 79%). At 120 mm, CPM predicts an average temperature 8 °C higher than the field model, yet COS conversions remain nearly identical at 90% and 89%, respectively.

These results indicate that, regardless of whether the CPM or LFM is used, the overall trends in temperature and COS conversion remain consistent. The temperature and reactant conversion predicted by the LFM exhibit the same behavior as seen in Fig. 6 for the relative deviation in total power and for linear power density predictions. Notably, the relative temperature and conversion predictions shift with increasing electrode submersion depth. Initially, the CPM underpredicts temperature and conversion compared to the LFM. However, as the electrode is submerged deeper, it transitions to an overprediction.

The shift from underprediction to overprediction in temperature and conversion arises primarily from how differences in the Joule heating profiles translate into thermal and reactive behavior. Since temperature is governed by the balance between Joule heating and heat of reaction, any deviations in power density directly influence the predicted temperature profile. In case of more shallow submersion, the partition-based model underestimates Joule heating in the region below the electrode tip, leading to lower overall temperature predictions. This, in turn, reduces the reaction rate. However, upon deeper submersion, the truncated cone approximation in the partition-based model begins to concentrate power more intensely than the LFM in the same region, causing it to overpredict the temperature. The higher temperature enhances reaction kinetics, driving conversion slightly above the LFM predictions despite similar power inputs at deeper submersions. Thus, while both models capture the general trends in temperature and conversion, their assumptions about Joule heating distribution lead to systematic deviations in temperature and conversion predictions.

The temperature increase in the CPM between each simulation closely follows the geometric quadratic increase in Joule heating predicted by the truncated cone representation (see Fig. 4, right). As the submersion depth increases, the linear power density profile of the TCR leads to a nonlinear rise in the average temperature. This explains why temperature increments become progressively larger at deeper submersions in the CPM. In contrast, in the LFM, the temperature increases are more evenly spaced. This is because the LFM accounts for a more gradual spatial distribution of Joule heating, rather than concentrating it only due to geometric variations within a confined region below the electrode tip. As a result, the temperature increases between each simulation profile exhibits a more linear-like progression with increasing submersion depth. This distinction between the two models reinforces how the assumed power distribution affects thermal predictions, with the CPM leading to steeper temperature increases at greater submersion depths due to the geometric dependence of the TCR.

In both models, higher temperatures lead to higher superficial velocities and improved mixing, as evidenced by the conversion profiles. The increase in temperature due to deeper electrode submersion causes gas expansion, which raises u and reduces tr. Despite the shorter residence time potentially limiting reaction progress, the enhanced mixing and faster kinetics due to higher temperatures offset this effect, leading to improved conversion.

The choice between the LFM and the CPM involves a trade-off between computational cost and model accuracy. The LFM offers a more physically accurate representation of power distribution by solving the electric potential as a continuous field, capturing local variations in current flow, potential gradients, and electrode effects with higher precision. This increased accuracy allows for a more detailed understanding of how power generation varies within the reactor, which can be crucial for reactions with pronounced sensitivity to local temperature variations. However, this accuracy comes at a significant computational cost, as solving the field equations requires fine spatial discretization and iterative numerical methods, rendering it computationally much more expensive and time-consuming than the CPM. The computational cost of the LFM becomes particularly relevant when it is used in combination with an iterative simulation framework, where unknown

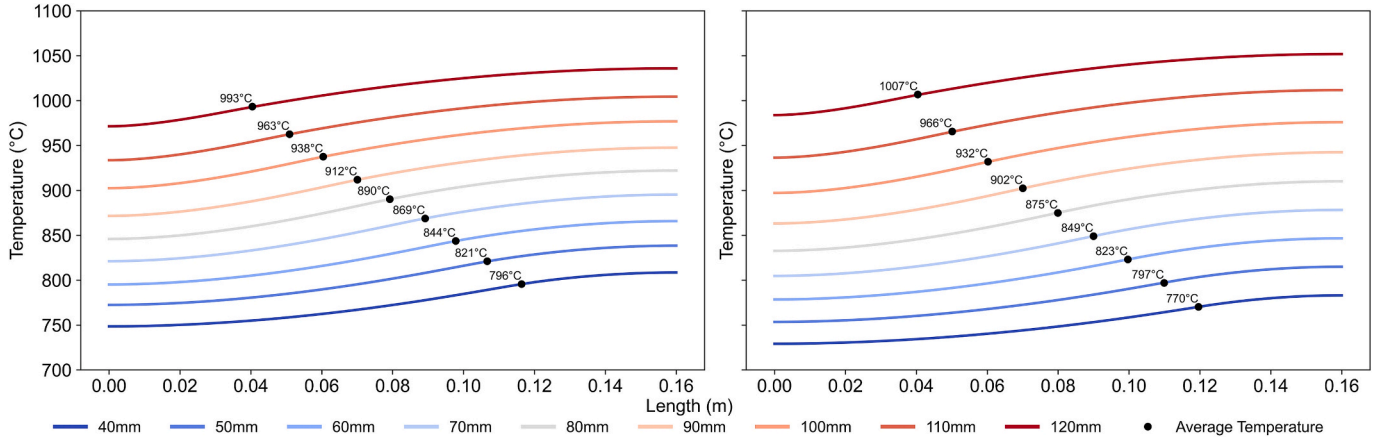

Fig. 12. Temperature profiles as a function of reactor length. (left) As predicted by the Laplacian Field model (LFM). right: As predicted by the Current Partition Model (CPM).

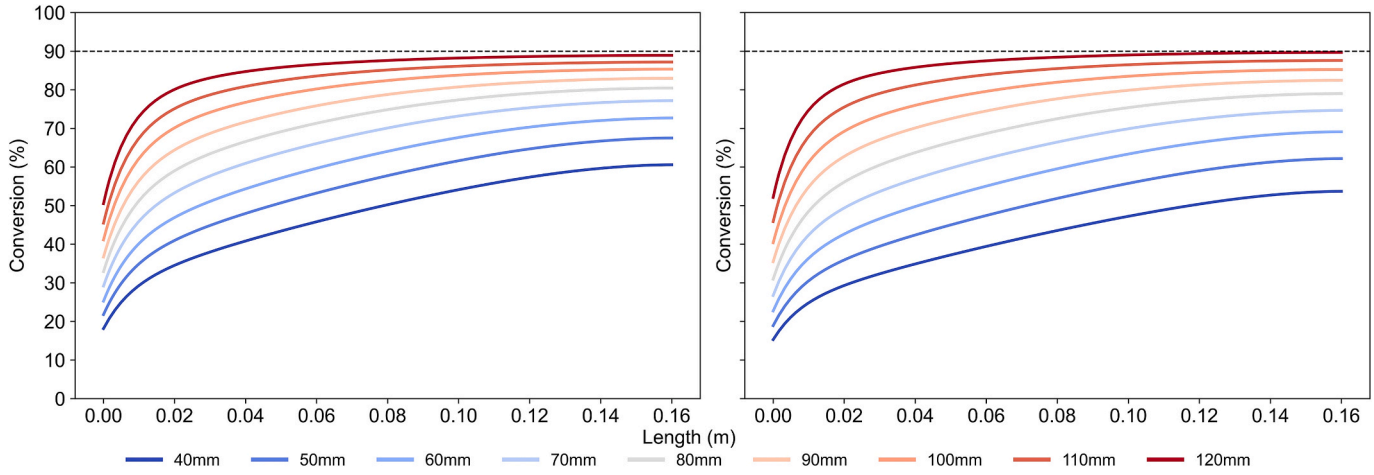

Fig. 13. COS decomposition conversion profiles as a function of reactor length. (left) As predicted by the Laplacian Field model (LFM). right: As predicted by the Current Partition Model (CPM).

parameters such as the average bed temperature, average conversion, or even the expanded bed height are solved together with the heat and mass balances. In such cases, the electric potential field is recomputed at each iteration, since the bed resistivity and height influence the spatial power density distribution. Using a refined grid and a standard Gauss-Seidel solver, solving the Laplacian field alone can take 2–10 min or more, depending on grid resolution and the convergence strategy (e.g., Successive Over Relaxation). In contrast, the full solution of the heat and mass balances with SciPy's solve_bvp for the CPM typically requires 5–20 iterations to converge the unknowns (e.g., average temperature to within 0.01 K). In practical runs with good initial guesses, the full simulation often completes in under 1 min, resulting in a significant computational advantage if the field is not re-solved each time.

If the bed height and resistivity are fixed, the Laplacian field only needs to be solved once at the start, which considerably reduces the total simulation time. However, when these parameters are dynamically updated, the electric potential must be re-solved at every iteration, significantly increasing computational effort.

By contrast, the CPM avoids solving the potential field numerically altogether. Power densities are computed from analytical expressions, enabling simulations to complete in the scale of seconds in typical cases. However, when the system becomes stiff (e.g., due to sharp temperature gradients or poorly chosen initial guesses), the boundary value problem solver may require up to 5 min to converge. In some cases, especially if the initial assumptions are far from the true solution or if tight error tolerances are imposed, the solver may fail to converge altogether or diverge into unphysical runaway solutions. As such, while the CPM offers clear advantages in terms of computational efficiency, its robustness and reliability depend significantly on solver configuration and initial conditions.

Overall, the CPM is well-suited for rapid parametric sweeps and qualitative exploration, whereas the LFM provides a more reliable and quantitative basis for rigorous analyses, particularly in contexts requiring accurate thermal profiles and energy estimates such as TEA or LCA.

4. Conclusions

A systematic methodology has been developed to simplify the simulation of the complex electrothermal behavior of fluidized beds containing electrically conductive particles. By expressing power generation in terms of fundamental electrical quantities, electric potential and current, the model provides a physically grounded interpretation of Joule heating mechanisms. Central to this approach is the field-resolved Laplacian model (LFM), which captures spatially varying electric fields and current paths, allowing for accurate predictions of power density distributions. This model provides a high-resolution framework that is particularly valuable for quantitative analyses involving endothermic reactions and temperature-sensitive processes.

To facilitate rapid qualitative analyses, an analytically simplified Current Partition Model (CPM) with reduced computational cost was also developed. This model approximates the reactor as a series of idealized resistive regions. While the CPM efficiently captures dominant trends and supports early-stage reactor design or parametric exploration, its accuracy diminishes under extreme geometries or when strong spatial heterogeneities influence the electric field. Still, within practical electrode configurations, it remains a reliable approximation. Specifically, in a central parameter region, electrode widths between 10% and 90% of the reactor radius and submersion depths between 20% and 80% of the bed height, CPM predictions of total Joule heating remain within $\pm$ 20% of LFM results. This deviation narrows to $\pm$ 10% in the more typical range of 20% to 70% width and 30% to 70% submersion, reflecting the CPM's robustness under realistic conditions. Outside these bounds, discrepancies become more pronounced due to the model's limited ability to capture complex current distribution, underscoring the importance of selecting the appropriate model based on the application.

Taken together, the LFM and CPM provide a systematic reactor-scale formulation for incorporating Joule heating into the energy balance of an ETFB. The aim of this formulation is not to construct the most detailed or fully resolved description of fluidized-bed hydrodynamics, but rather to establish a transparent and physically grounded way of representing how electrical design choices translate into spatially distributed heat generation. By expressing Joule heating directly through potential and current fields, the framework avoids empirical tuning and clarifies the link between geometry, electrical configuration, and thermal response. This reactor-scale perspective enables systematic evaluation of ETFB behavior while remaining compatible with future extensions toward more detailed hydrodynamic models.

An initial thermal model assessment against reported ETFB heating data demonstrated that the framework can reproduce electrode-tip temperature trends within $\pm$ 50 °C when effective resistivity and heat-loss closures are calibrated. The results highlight the strong sensitivity of ETFB predictions to electrical boundary assumptions and the need for improved characterization of intrinsic bed resistivity and contact losses.

In applying this methodology to COS decomposition, both the LFM and CPM yield temperature and conversion profiles that follow the expected behavior of a bubbling fluidized bed with strong axial mixing. According to both models, the thermal profiles shift upward upon deeper electrode submersion, consistent with the movement of the heating zone toward the bed surface. However, the LFM, by resolving

the full 2D electric potential field, more realistically captures the continuous distribution of Joule heating, providing a smoother and more physically coherent response to geometric changes. Notably, the average temperature in the LFM varies more linearly with electrode submersion depth, reflecting the fixed resistivity and the direct scaling of power distribution. In contrast, the CPM exhibits increasing deviations in average temperature with deeper submersion, driven by the non-linear nature of the truncated cone resistor approximation. This discrepancy underscores the limitations of the geometric partitioning approach when used to model spatially distributed phenomena and highlights the value of the LFM for quantitatively consistent thermal and reactive predictions.

In the e-CODUCT context, the modelling framework developed here can be used as a reactor-scale design tool to translate process targets into ETFB sizing and configuration choices. For a specified duty (throughput) and performance criterion, e.g., a target COS conversion associated with a desired CO and sulfur production rate, the coupled electrical–thermal–reactive formulation enables systematic selection of reactor diameter, bed volume/height, and electrode geometry/position to deliver the required spatial distribution of Joule heating while maintaining a consistent bubbling-bed hydrodynamic regime. In this way, the framework provides a structured basis for early-stage design iterations that connect electrical design variables (electrode placement, submersion depth, and current paths) to heat demand and temperature profiles, and ultimately to achievable conversion levels and reactor sizing requirements for electrified, endothermic COS reaction. The model further provides a direct estimate of the minimum Joule-heating duty required to sustain endothermic conversion, offering practical guidance for power-supply sizing and reactor design.

Although the CPM reproduces the overall qualitative trends, the LFM's spatial resolution captured the localized heating effects that strongly affect temperature and conversion profiles. The trade-off between the two approaches was further illustrated by their computational performance: the LFM, when solving the Laplacian field with a Gauss-Seidel scheme on a refined grid, requires 2–10 min per solution, with total convergence times between 15 s and 2 min depending on the unknown inputs. If bed resistivity and height are fixed, the LFM must only be solved once, significantly reducing computation time. On the other hand, the CPM typically converges within seconds, but may require up to 5 min if initial guesses are poor or if tolerances are tight, and may even fail to converge under highly stiff conditions.

This work emphasizes that the choice of model is not merely about computational convenience but has implications for model fidelity, interpretability, and predictive power. While computationally more demanding, the Laplacian field model provides essential spatial insights and higher quantitative accuracy, particularly valuable for engineering design, optimization, and rigorous reactor performance evaluation.

Funding information

This work was supported by the European Union's Horizon Europe research and innovation program under Grant Agreement No. 101058100 (e-CODUCT project). The authors gratefully acknowledge this funding support.

CRediT authorship contribution statement

Klaus Jacobs: Writing – original draft, Visualization, Methodology, Investigation, Formal analysis, Data curation, Conceptualization. **Soroush Zareghorbaei:** Writing – review & editing, Visualization, Validation, Methodology, Investigation, Formal analysis, Data curation. **Jeroen Lauwaert:** Writing – review & editing, Supervision, Resources, Project administration, Conceptualization. **Joris W. Thybaut:** Writing – review & editing, Supervision, Resources, Project administration, Funding acquisition, Conceptualization.

Declaration of competing interest

The authors declare that they have no known competing financial interests or personal relationships that could have appeared to influence the work reported in this paper.

Appendix A. Supplementary data

Supplementary data to this article can be found online at https://doi.org/10.1016/j.ces.2026.123647.

Data availability

Data will be made available on request.

References

Abba, I., 2001. A generalized fluidized bed reactor model across the flow regimes. Univ. Br. Columbia. https://doi.org/10.14288/1.0058662.
Abba, I.A., Grace, J.R., Bi, H.T., Thompson, M.L., 2003. Spanning the flow regimes: generic fluidized-bed reactor model. AIChE J. 49, 1838–1848. https://doi.org/10.1002/AIC.690490720.
Abrahamsen, A.R., Geldart, D., 1980. Behaviour of gas-fluidized beds of fine powders part I homogeneous expansion. Powder Technol. 26, 35–46. https://doi.org/10.1016/0032-5910(80)85005-4.
Agu, C.E., Pfeifer, C., Eikeland, M., Tokheim, L.A., Moldestad, B.M.E., 2018. Models for predicting average bubble diameter and volumetric bubble flux in deep fluidized beds. Ind. Eng. Chem. Res. 57, 2658–2669. https://doi.org/10.1021/ACS.IECR.7B04370/ASSET/IMAGES/MEDIUM/IE-2017-04370G_M060.GIF.
I. Ahmed, S. Fedorov, A. Sybir, S. Hubynskyi, M. Duchesne, Electrically Heated Fluidized Bed for Graphite Purification: Heat Transfer and Electric Resistivity Models for Scale-Up, Metallurgical and Materials Transactions B 2025 56:6 56 (2025) 7150–7166. https://doi.org/10.1007/S11663-025-03758-7.
Ahmed, I., Duchesne, M., Tan, Y., Lu, D.Y., 2024. Electrically heated fluidized beds—a review. Ind. Eng. Chem. Res. 63, 4205–4235. https://doi.org/10.1021/ACS.IECR.3C04232/ASSET/IMAGES/LARGE/IE3C04232_0023.JPEG.
Akimoto, M., Suto, H., Niiyama, H., 1986. Preparation of solid catalysts for vapor-phase decomposition of carbonyl sulfide. Bull. Chem. Soc. Jpn 59, 683–687. https://doi.org/10.1246/BCSJ.59.683.
Atuonwu, J.C., Tassou, S.A., 2018. Quality assurance in microwave food processing and the enabling potentials of solid-state power generators: a review. J. Food Eng. 234, 1–15. https://doi.org/10.1016/j.jfoodeng.2018.04.009.
Bi, H.T., Grace, J.R., 1997. Axial dispersion and interphase transfer in turbulent fluidized beds. Internal Report, Vancouver.
Breault, R.W., 2006. A review of gas–solid dispersion and mass transfer coefficient correlations in circulating fluidized beds. Powder Technol. 163, 9–17. https://doi.org/10.1016/J.POWTEC.2006.01.009.
Butland, A.T.D., Maddison, R.J., 1973. The specific heat of graphite: an evaluation of measurements. J. Nucl. Mater. 49, 45–56.
Chen, J.C., Grace, J.R., Golriz, M.R., 2005. Heat transfer in fluidized beds: design methods. Powder Technol. 150, 123–132. https://doi.org/10.1016/J.POWTEC.2004.11.035.
Clark, P.D., Dowling, N.I., Huang, M., Svrcek, W.Y., Monnery, W.D., 2001. Mechanisms of CO and COS formation in the Claus furnace. Ind. Eng. Chem. Res. 40, 497–508. https://doi.org/10.1021/IE990871L/ASSET/IMAGES/LARGE/IE990871LH00005.JPEG.
R. Clift, JR. Grace, CONTINUOUS BUBBLING AND SLUGGING., in: Fluidization, 2nd ed., Academic Press, 1985: pp. 73–132.
e-CODUCT – Greenhouse gas and acid gases conversion by electrothermal catalysis, (n. d.). https://e-coduct.eu/ (accessed July 28, 2025).
M. Fabbiani, V. Bikbaeva, L. Pinard, A. Novikov, H. Retot, V. Valtchev, Alternative to Claus process through COS as intermediate. Part 1: CO2 and H2S competitive adsorption on zeolite 13X, in: A. Bouriakova (Ed.), "CAMURE 12 & ISMR 11, Abstracts." 2024., UGent, Gent, 2024: pp. 165–166.
Fedorov, S.S., Rohatgi, U.S., Barsukov, I.V., Gubynskyi, M.V., Barsukov, M.G., Wells, B. S., Livitan, M.V., Gogotsi, O.G., 2016. Ultra-high Temperature continuous reactors based on electrothermal fluidized bed concept. J. Fluids Eng. Trans. ASME 138, 044502. https://doi.org/10.1115/1.4031689.
Feng, F., Song, G.H., Shen, L.H., Xiao, J., 2016. Energy efficiency analysis of biomass-based synthetic natural gas production process using interconnected fluidized beds and fluidized bed methanation reactor, Clean Technol. Environ. Policy 18, 965–971. https://doi.org/10.1007/S10098-015-1069-8/TABLES/4.
Gao, W., Kong, L., Hodgson, P., 2014. Fluidized-bed heat treating equipment. Steel Heat Treat. Technol. 233–241. https://doi.org/10.31399/ASM.HB.V04B.A0005927.
Goldschmidt, D., Le Goff, P., 1963. Resistance electrique des lits fluidises - I. Resistances moyennes de grains conducteurs fluidises par air - resultats preliminaires. Chem. Eng. Sci. 18, 805–806. https://doi.org/10.1016/0009-2509(63)85047-2.
Graham, W., Harvey, E.A., 1965. The electrical resistance of fluidized beds of coke and graphite. Can. J. Chem. Eng. 43, 146–149. https://doi.org/10.1002/CJCE.5450430310.

Gubinskyi, M., Fiodorov, S., Kremniova, Y., Gogotsi, O., Vvedenska, T., 2017. Mathematical modelling of electric conductivity of dense and fluidized beds. In: Power Engineering and Information Technologies in Technical Objects Control, 1st ed.,. Informa UK Limited, pp. 173–180. https://doi.org/10.1201/9781315197814-22.

C.K.. Gupta, D. Sathiyamoorthy, Fluid bed technology in materials processing, (1999) 498.

Haas, L.A., Khalafalla, S.E., 1973. Catalytic thermal decomposition of carbonyl sulfide and its reaction with sulfur dioxide. J. Catal. 30, 451–459. https://doi.org/10.1016/0021-9517(73)90163-2.

Hay, A.J., Belford, R.L., 1967. High-temperature gas-kinetic study of carbonyl sulfide pyrolysis performed with a shock tube and quadrupole mass filter. J. Chem. Phys. 47, 3944–3960. https://doi.org/10.1063/1.1701558.

How electrification can help industrial companies cut costs | McKinsey, (n.d.). https://www.mckinsey.com/industries/electric-power-and-natural-gas/our-insights/plugging-in-what-electrification-can-do-for-industry (accessed January 28, 2025).

Idakiev, V.V., Steinke, C., Sondej, F., Bück, A., Tsotsas, E., Mörl, L., 2018. Inductive heating of fluidized beds: spray coating process. Powder Technol. 328, 26–37. https://doi.org/10.1016/j.powtec.2018.01.017.

Johnson, H.S., 1961. Reactions in a fluidized coke bed with self-resistive heating. Can. J. Chem. Eng. 39, 145–147. https://doi.org/10.1002/CJCE.5450390309.

Jones, A.L., Wheelock, T.D., 1970. The electrical resistivity of fluidized carbon particles: significant parameters. Chem. Eng. Prog. Symp. Ser. 66, 157–166.

Karan, K., Mehrotra, A.K., Behie, L.A., 1998. COS-forming reaction between CO and sulfur: a high-temperature intrinsic kinetics study. Ind. Eng. Chem. Res. 37, 4609–4616. https://doi.org/10.1021/IE9802966.

Karan, K., Mehrotra, A.K., Behie, L.A., 2005. Thermal decomposition of carbonyl sulfide at temperatures encountered in the front end of modified claus plants. Chem. Eng. Commun. 192, 370–385. https://doi.org/10.1080/00986440590477764.

Kavlick, V.J., Lee, B.S., Schora, F.C., 1971. Electrothermal coal char gasification. [High-temperature, high-pressure synthesis gas manufactured by steam gasification of coal char]. AIChE Symp. Ser. 67, 116.

Knowlton, T.M., 1971. Components of Interelectrode Resistance in an Electrofluid Bed Reactor. Iowa State University.

D. Kunii, O. Levenspiel, Fluidization Engineering 2nd Edition, (2013) 491. http://www.sciencedirect.com:5070/book/9780080506647/fluidization-engineering?via=ihub= (accessed July 9, 2025).

M. Lungu, J. Sun, J. Wang, Z. Zhu, Y. Yang, Computational fluid dynamics simulations of interphase heat transfer in a bubbling fluidized bed, Korean Journal of Chemical Engineering 2014 31:7 31 (2014) 1148–1161. https://doi.org/10.1007/S11814-014-0022-6.

M. V. Gubynskyi, I. V. Barsukov, O.G. Gogotsi, S.S. Fedorov, M. V. Livitan, U. Rohatgi, Electrothermal Fluidized Bed Furnace for Thermal Treatment of Recycled Battery Wastes, American Society of Mechanical Engineers, Fluids Engineering Division (Publication) FEDSM 1 B (2013). https://doi.org/10.1115/FEDSM2013-16630.

A.I. Malinovskii, O.S. Rabinovich, V.A. Borodulya, A.Z. Greben'kov, A.M. Sidorovich, Local conductivity of a fluidized bed consisting of conducting particles, Journal of Engineering Physics and Thermophysics 85 (2012) 251–258. https://doi.org/10.1007/S10891-012-0647-4.

Oya, M., Shiina, H., Tsuchiya, K., Matsui, H., 1994. Thermal decomposition of cos. Bull. Chem. Soc. Jpn 67, 2311–2313. https://doi.org/10.1246/BCSJ.67.2311.

Partington, J.R., Neville, H.H., 1951. 274. the thermal decomposition of carbonyl sulphide. J. Chem. Soc. (resumed) 1230–1237. https://doi.org/10.1039/JR9510001230.

Pulsifer, A.H., Wheelock, T., 1978. The electrical resistance of gas fluidized beds. Fluidization 76–80.

Reid, R.C., Prausnitz, J.M., Poiling, B.E., 1987. The properties of gases and Liquids, 4th ed. McGraw-Hill, New York.

Sakr, M., Liu, S., 2014. A comprehensive review on applications of ohmic heating (OH). Renew. Sustain. Energy Rev. 39, 262–269. https://doi.org/10.1016/J.RSER.2014.07.061.

Saygin, D., Gielen, D., 2021. Zero-emission pathway for the global chemical and petrochemical sector. Energies (basel). 14, 3772. https://doi.org/10.3390/EN14133772/S1.

Schecker, H.G., Wagner, H.G., 1969. On the thermal decomposition of COS. Int. J. Chem. Kinet. 1, 541–549. https://doi.org/10.1002/KIN.550010605.

Seo, Y.S., Mohamed, A.A.H., Woo, K.C., Lee, H.W., Lee, J.K., Kim, K.T., 2010. Comparative studies of atmospheric pressure plasma characteristics between He and Ar working gases for sterilization. IEEE Trans. Plasma Sci. 38, 2954–2962. https://doi.org/10.1109/TPS.2010.2058870.

Siesing, L., Lundström, F., Frogner, K., Cedell, T., Andersson, M., 2018. Towards energy efficient heating in industrial processes - three steps to achieve maximized efficiency in an induction heating system, in. Procedia Manuf., Elsevier b.v. 404–411. https://doi.org/10.1016/j.promfg.2018.06.110.

Simeiko, K.V., 2018. Development and verification of appropriateness for mathematical model of heat balance of electrothermal fluidized bed reactor. Thermophys. Therm. Power Eng. 41, 35–40. https://doi.org/10.31472/TTPE.2.2019.5.

Sit, S.P., Grace, J.R., 1981. Effect of bubble interaction on interphase mass transfer in gas fluidized beds. Chem. Eng. Sci. 36, 327–335. https://doi.org/10.1016/0009-2509(81)85012-9.

Song, G., Zhao, S., Wang, X., Cui, X., Wang, H., Xiao, J., 2022. An efficient biomass and renewable power-to-gas process integrating electrical heating gasification. Case Stud. Therm. Eng. 30. https://doi.org/10.1016/j.csite.2021.101735.

Stankiewicz, A.I., Nigar, H., 2020. Beyond electrolysis: old challenges and new concepts of electricity-driven chemical reactors, React. Chem. Eng. 5, 1005–1016. https://doi.org/10.1039/D0RE00116C.

Thompson, M.L., Bi, H., Grace, J.R., 1999. A generalized bubbling/turbulent fluidized-bed reactor model. Chem. Eng. Sci. 54, 2175–2185. https://doi.org/10.1016/S0009-2509(98)00354-6.

Use of energy in industry - U.S. Energy Information Administration (EIA), (n.d.). https://www.eia.gov/energyexplained/use-of-energy/industry.php (accessed October 8, 2024).

Walker, R.E., Westenberg, A.A., 1960. Molecular Diffusion Studies in gases at High Temperature. IV. results and Interpretation of the CO2–O2, CH4–O2, H2–O2, CO–O2, and H2O–O2 Systems. J. Chem. Phys. 32, 436–442. https://doi.org/10.1063/1.1730712.

D. Woiki, P. Roth, Shock Tube Measurements on the Thermal Decomposition of COS, Berichte Der Bunsengesellschaft Für Physikalische Chemie 96 (1992) 1347–1352. https://doi.org/10.1002/BBPC.19920961005.

Wong, D.S.H., Sandler, S.I., 1992. A theoretically correct mixing rule for cubic equations of state. AIChE J 38, 671–680. https://doi.org/10.1002/AIC.690380505.

Yoshida, K., Kunii, D., 1968. Stimulus and response of gas concentration in bubbling fluidized beds. J. Chem. Eng. Jpn. 1, 11–16. https://doi.org/10.1252/JCEJ.1.11.

Zhang, Y., Lu, C., Shi, M., 2009. Evaluating solids dispersion in fluidized beds of fine particles by gas backmixing experiments. Chem. Eng. Res. Des. 87, 1400–1408. https://doi.org/10.1016/J.CHERD.2009.03.010.